ATLAS CONF Note

ATLAS-CONF-2020-039

31st July 2020

Search for charged Higgs bosons decaying into a top-quark and a bottom-quark at $\sqrt{s} = 13$ TeV with the ATLAS detector

The ATLAS Collaboration

A search for charged Higgs bosons decaying into a top-quark and a bottom-quark is presented. The data analysed correspond to 139 fb^{-1} of proton-proton collisions at $\sqrt{s} = 13$ TeV, recorded with the ATLAS detector at the LHC. The production of a heavy charged Higgs boson in association with a top-quark and a bottom-quark, $pp \to tbH^+ \to tbtb$, is explored in the H^+ mass range from 200 to 2000 GeV using final states with jets and one electron or muon. Events are categorised according to the multiplicity of jets and b-tagged jets, and multivariate techniques are used to further discriminate between signal and background events. No significant excess above the background-only hypothesis is observed and exclusion limits are derived for the production cross-section times branching ratio of a charged Higgs boson as a function of its mass, which range from 3.6 pb at 200 GeV to 0.035 pb at 2000 GeV at 95% CL. The results are interpreted in the hMSSM and M_h^{125} scenarios.

ATLAS-CONF-2020-039
12 August 2020

1 Introduction

The discovery of a Higgs boson with a measured mass close to 125 GeV at the Large Hadron Collider (LHC) in 2012 [1–3], raises the question of whether this is the Higgs boson of the Standard Model (SM), or part of an extended scalar sector. Charged Higgs bosons[1] are predicted in several extensions of the SM that add a second doublet [4–7] or triplets [8–12] to the scalar sector. In CP-conserving two-Higgs-doublet models (2HDMs), the properties of the charged Higgs boson depend on its mass, the mixing angle α of the neutral CP-even Higgs bosons, and the ratio of the vacuum expectation values of the two Higgs doublets ($\tan\beta$). This analysis searches for charged Higgs bosons heavier than the top-quark and decaying to a top-quark and a bottom-quark. In this mass range the primary production mechanism at the LHC is expected to be in association with a top-quark and a bottom-quark, as illustrated in Figure 1.

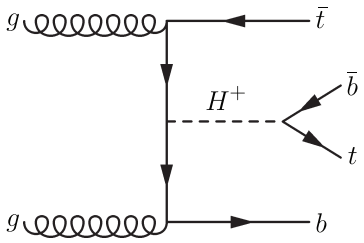

Figure 1: Leading-order Feynman diagram for the production of a heavy charged Higgs boson in association with a top-quark and a bottom-quark, as well as its decay to a top-quark and a bottom-quark.

The ATLAS and CMS collaborations have searched for charged Higgs bosons in pp collisions at $\sqrt{s} = 7, 8$ and 13 TeV with data samples varying from 2.9 to 36 fb^{-1}, probing the mass range below the top-quark mass in the $\tau\nu$ [13–18], cs [19, 20], and cb [21] decay modes, as well as above the top-quark mass in the $\tau\nu$ and tb decay modes [15, 17, 18, 22–26]. In addition, $H^+ \to WZ$ was searched for in the vector-boson-fusion production mode [27, 28]. ATLAS has also set limits on the H^+ production in a search for dijet resonances in events with an isolated lepton using the Run 2 dataset [29]. No evidence for charged Higgs bosons was found in any of these searches.

This paper presents an updated search for H^+ production in the $H^+ \to tb$ decay mode with the full Run 2 dataset of pp collisions taken at $\sqrt{s} = 13$ TeV. This decay mode has the highest branching ratio for charged Higgs bosons above the top quark mass. Events with one charged lepton ($l = e, \mu$) and jets in the final state are considered, and exclusive regions are defined according to the overall number of jets, and the number of jets tagged as containing a b-hadron. In order to separate signal from SM background, multivariate analysis techniques (MVA) combining several kinematic variables are employed in the regions where the signal rate is expected to be largest. Limits to the $pp \to tbH^+$ production cross-section times the $H^+ \to tb$ branching ratio are set by means of a simultaneous fit to the MVA classifier outputs in the different analysis regions, which determines both the contribution from the $H^+ \to tb$ signal and the normalisation of the backgrounds. The results are interpreted in the framework of the hMSSM [30–33] and various M_h^{125} benchmark scenarios of the Minimal Supersymmetric Standard Model (MSSM) [34–39].

This paper is organised as follows. In Section 2, the data and samples of simulated events used in the analysis are summarised. The reconstruction of objects in ATLAS and the event selection are described in

[1] For simplicity in the following, charged Higgs bosons are denoted H^+, with the charge-conjugate H^- always implied. Similarly, the difference between quarks and anti-quarks q and $\bar{q}$ is generally understood from the context, so that e.g. $H^+ \to tb$ means both $H^+ \to t\bar{b}$ and $H^- \to \bar{t}b$.

Section 3, and the background modelling is discussed in Section 4. The analysis strategy is presented in Section 5 and systematic uncertainties in Section 6. Section 7 includes the results of the fit, the exclusion limits in terms of cross section times branching ratio, and their interpretation in several benchmark scenarios. Finally, a summary is given in Section 8.

2 Data and simulation samples

The data used in this analysis were recorded with the ATLAS detector at the LHC between 2015 and 2018 from $\sqrt{s} = 13$ TeV pp collisions, and correspond to an integrated luminosity of 139 fb^{-1}. ATLAS [40] is a multi-purpose detector with a forward-backward symmetric cylindrical geometry and a near 4π coverage in solid angle[2]. It consists of an inner tracking detector (ID) surrounded by a thin superconducting solenoid providing a 2 T axial magnetic field, electromagnetic and hadron calorimeters, and a muon spectrometer (MS). The inner tracking detector covers the pseudorapidity range $|\eta| < 2.5$. It consists of silicon pixel, silicon microstrip, and transition radiation tracking detectors. Lead/liquid-argon (LAr) sampling calorimeters provide electromagnetic (EM) energy measurements with high granularity. A hadron (steel/scintillator-tile) calorimeter covers the central pseudorapidity range ($|\eta| < 1.7$). The end-cap and forward regions are instrumented with LAr calorimeters for both EM and hadronic energy measurements up to $|\eta| = 4.9$. The muon spectrometer surrounds the calorimeters and is based on three large air-core toroidal superconducting magnets with eight coils each. The field integral of the toroids ranges between 2.0 and 6.0 T m across most of the detector. The muon spectrometer includes a system of precision tracking chambers and fast detectors for triggering. Only runs with stable colliding beams in which all relevant detector components were functional are used.

A two-level trigger system, with the first level implemented in custom hardware and followed by a software-based second level, is used to reduce the trigger rate to around 1 kHz for offline storage [41]. Events in this analysis were recorded using single-lepton triggers. To maximise the event selection efficiency, multiple triggers were used, either with low p_{T} thresholds and lepton identification and isolation requirements, or with higher p_{T} thresholds but looser identification criteria and no isolation requirements. Slightly different sets of triggers were used for 2015 and 2016-2018 data due to the increase of the average number of interactions per bunch crossing (pile-up). The minimum p_{T} required to the triggers was increased to keep both trigger rate and data storage within their limits. For muons, the lowest p_{T} threshold was 20 (26) GeV in 2015 (2016-2018), while for electrons, triggers with a p_{T} threshold of 24 (26) GeV were used [42]. Simulated events are also required to satisfy the trigger criteria. Signal and background processes are modelled with Monte Carlo (MC) simulation samples. The $pp \to tbH^+$ followed by $H^+ \to tb$ process is modelled with MadGraph5_aMC@NLO [35] at next-to-leading order (NLO) in QCD [43] using a four-flavour scheme (4FS) implementation with the NNPDF2.3NLO [44] parton distribution function (PDF). Parton shower (PS) and hadronisation are modelled by Pythia 8.212 [45] with the A14 [46] set of underlying event (UE) related parameters tuned to ATLAS data (tune). Dynamic QCD factorisation and renormalisation scales, μ_f and μ_r, are set to $\frac{1}{3}\sum_i \sqrt{m(i)^2 + p_{\mathrm{T}}(i)^2}$, where i runs over the final state particles (H^+, t and b) used in the generation. Only the H^+ decay into tb is considered. For the simulation of the tbH^+ process the narrow-width approximation is used. This assumption has a negligible impact on

[2] ATLAS uses a right-handed coordinate system with its origin at the nominal interaction point (IP) in the centre of the detector and the z-axis along the beam pipe. The x-axis points from the IP to the centre of the LHC ring, and the y-axis points upwards. Cylindrical coordinates (r, ϕ) are used in the transverse plane, ϕ being the azimuthal angle around the z-axis. The pseudorapidity is defined in terms of the polar angle θ as $\eta = -\ln\tan(\theta/2)$. Angular distance is measured in units of $\Delta R \equiv \sqrt{(\Delta\eta)^2 + (\Delta\phi)^2}$.

the analysis for the models considered in this paper, as the experimental resolution is much larger than the H^+ natural width. Interference with the SM $t\bar{t}b\bar{b}$ background is neglected. A total of 18 H^+ mass hypotheses are used, with 25 GeV mass steps between an H^+ mass of 200 GeV and 300 GeV, 50 GeV steps between 300 GeV and 400 GeV, 100 GeV steps between 400 GeV and 1000 GeV and 200 GeV steps from 1000 GeV to 2000 GeV. The step sizes are selected to match the experimental resolution of the H^+ signal.

The production of $t\bar{t}$ + jets events is modelled using the PowhegBox [47–50] v2 generator, which provides matrix element (ME) at NLO in QCD, with the NNPDF3.0NLO PDF set [51]. The h_{damp} parameter, which controls the transverse momentum of the first additional emission beyond the Born configuration, was set to $1.5m_t$ [52], where m_t is the mass of the top-quark. Parton shower and hadronisation were modelled by Pythia 8.230 [53] with the A14 UE tune. The scales μ_f and μ_r are set to the default scale $\sqrt{m_t^2 + p_{\text{T},t}^2}$. The sample was normalised to the Top++ 2.0 [54] theoretical cross-section of 832^{+46}_{-51} pb, calculated at next-to-next-to-leading order (NNLO) in QCD including resummation of next-to-next-to leading logarithmic (NNLL) soft gluon terms [55–58]. The generation of the $t\bar{t}$ + jets events was performed both inclusively of additional jet flavour, and also with dedicated filtered samples, requiring b- or c-hadrons in addition to those arising from the decays of the top-quarks. Events generated with no extra b-hadrons are taken from the unfiltered sample and merged with the $t\bar{t}$ + jets events from the filtered sample, taking the appropriate cross-section and filter efficiencies into account.

Single-top t-channel production is modelled using the PowhegBox v2 generator in the 4FS with the NNPDF3.0NLOnf4 PDF set [51]. The scales μ_f and μ_r are set to $\sqrt{m_b^2 + p_{\text{T},b}^2}$ following the recommendation in Ref. [59]. Single-top tW and s-channel production are modelled using the PowhegBox v2 generator in the five-flavour scheme (5FS) with the NNPDF3.0NLO PDF set. The scales μ_f and μ_r are set to the default scale, which is equal to the top-quark mass. For the tW associated production, the diagram removal scheme [60] was employed to handle the interference with $t\bar{t}$ production [52]. All single top events are showered with Pythia 8.230.

Vector bosons with additional jets production is simulated with the Sherpa 2.2.1 MC generator. NLO-accurate ME for up to two jets, and leading order (LO)-accurate ME for up to four jets are calculated with the Comix [61] and OpenLoops [62, 63] libraries. The default Sherpa PS [64] based on Catani-Seymour dipoles and the cluster hadronisation model [65] are used. They employ the dedicated set of tuned parameters developed by the Sherpa authors for this version based on the NNPDF3.0NNLO PDF set. The NLO ME of a given jet-multiplicity are matched to the PS using a colour-exact variant of the MC@NLO algorithm [66]. Different jet multiplicities are then merged into an inclusive sample using an improved CKKW matching procedure [67, 68], which is extended to NLO accuracy using the MEPS@NLO prescription [69]. The merging cut is set to 20 GeV.

The production of $t\bar{t}V$ events, i.e. $t\bar{t}W$ or $t\bar{t}Z$, is modelled using the MadGraph5_aMC@NLO 2.3.3 generator, which provides ME at NLO in QCD with the NNPDF3.0NLO PDF set. The scales μ_f and μ_r are set to the default scale $\frac{1}{2} \times \sum_i \sqrt{m_i^2 + p_{\text{T}_i}^2}$, where the sum runs over all the particles generated from the ME calculation. The events are showered with Pythia 8.210. Additional $t\bar{t}V$ samples are produced with the Sherpa 2.2.0 [70] generator at LO accuracy, using the MEPS@LO prescription [67, 68] with up to one additional parton for the $t\bar{t}Z$ sample and two additional partons for $t\bar{t}W$. A dynamic μ_r is used, defined similarly to that of the nominal MadGraph5_aMC@NLO samples. The CKKW matching scale of the additional emissions is set to 30 GeV. The default Sherpa 2.2.0 PS is used along with the NNPDF3.0NNLO PDF set. The production of $t\bar{t}H$ events is modelled in the 5FS using the PowhegBox [71] generator at

NLO with the NNPDF3.0NLO PDF set. The h_{damp} parameter is set to $3/4 \cdot (2m_t + m_H) = 352.5$ GeV, and the events are showered with Pythia 8.230.

Diboson samples are simulated with the Sherpa 2.2 generator. Multiple ME calculations are matched and merged with the Sherpa PS using the MEPS@NLO prescription [64, 65]. For fully leptonically decaying diboson samples, as well as loop-induced diboson samples, the virtual QCD correction for ME at NLO accuracy are provided by the OpenLoops library. For electroweak $VVjj$ production, the calculation is performed in the G_μ-scheme [72], ensuring an optimal description of pure electroweak interactions at the electroweak scale. All samples are generated using the NNPDF3.0NNLO PDF set, along with the dedicated set of tuned PS parameters developed by the Sherpa authors.

Other minor backgrounds ($tHjb$, tHW, tZq, tZW and four top quarks) are also simulated and accounted for, even though they contribute less than 1% in any analysis region. All samples and their basic generation parameters are summarised in Table 1.

Table 1: Nominal simulated signal and background event samples. The ME generator, PS generator and calculation accuracy of the cross-section in QCD used for normalisation (aNNLO stands for approximate NNLO in QCD) are shown together with the applied PDF set. Either Sherpa 2.2.1 or Sherpa 2.2.2 has been used for different diboson contributions. The rightmost column shows whether fast or full simulation has been used to produce the samples.

Physics process	ME generator	PS generator	Normalisation	PDF set	Simulation
tbH^+	MG5_aMC 2.6.2	Pythia 8.212	NLO	NNPDF2.3NLO	Fast
$t\bar{t}$ + jets	PowhegBox v2	Pythia 8.230	NNLO+NNLL	NNPDF3.0NLO	Fast
Single top t-chan	PowhegBox v2	Pythia 8.230	aNNLO	NNPDF3.0NLOnf4	Full
Single top tW	PowhegBox v2	Pythia 8.230	aNNLO	NNPDF3.0NLO	Full
Single top s-chan	PowhegBox v2	Pythia 8.230	aNNLO	NNPDF3.0NLO	Full
V + jets	Sherpa 2.2.1	Sherpa 2.2.1	NNLO	NNPDF3.0NNLO	Full
$t\bar{t}V$	MG5_aMC 2.3.3	Pythia 8.210	NLO	NNPDF3.0NLO	Full
$t\bar{t}H$	PowhegBox v2	Pythia 8.230	NLO	NNPDF3.0NLO	Full
Diboson	Sherpa 2.2	Sherpa 2.2	NLO	NNPDF3.0NNLO	Full
$tHjb$	MG5_aMC 2.6.0	Pythia 8.230	NLO	NNPDF3.0NLOnf4	Full
tHW	MG5_aMC 2.6.2	Pythia 8.235	NLO	NNPDF3.0NLO	Full
tZq	MG5_aMC 2.3.3	Pythia 8.212	NLO	CTEQ6L1LO	Full
tZW	MG5_aMC 2.3.3	Pythia 8.212	NLO	NNPDF3.0NLO	Full
Four tops	MG5_aMC 2.3.3	Pythia 8.230	NLO	NNPDF3.1NLO	Fast

Most of the samples mentioned above were produced using the full ATLAS detector simulation [73] based on Geant4 [74], and the rest were produced using fast simulation [75], where the complete Geant4 simulation of the calorimeter response is replaced by a detailed parametrisation of the shower shapes, as shown in Table 1. For the observables used in this analysis, both simulations were found to give compatible results. Additional pile-up interactions, simulated with Pythia 8.186 using the A3 set of tuned parameters [52], were overlaid onto the simulated hard-scatter event. All simulation samples were reweighted such that the distribution of the number of pile-up interactions matches that of the data. In all samples the top-quark mass was set to 172.5 GeV, and the decays of b- and c-hadrons were performed by EvtGen v1.2.0 [76], except in samples simulated by the Sherpa event generator.

3 Object reconstruction and event selection

Charged leptons and jets, including those compatible with the hadronisation of b-quarks, are the main reconstructed objects used in this analysis and are detailed below. Electrons are reconstructed from energy clusters in the electromagnetic calorimeter associated with tracks reconstructed in the ID [77], and are required to have $|\eta| < 2.47$. Candidates in the calorimeter transition region ($1.37 < |\eta| < 1.52$) are excluded. Electrons must satisfy the *tight* identification criterion described in Ref. [78], based on shower-shape and track-matching variables. Muons are reconstructed from either track segments or full tracks in the MS which are matched to tracks in the ID. Tracks are then re-fit using information from both detector systems. Muons should satisfy the *medium* identification criterion [79]. Muons are required to have $|\eta| < 2.5$. To reduce the contribution of leptons from hadronic decays (non-prompt leptons), both the electrons and muons must satisfy isolation criteria. These criteria include both track and calorimeter information, and have an efficiency of 90% for leptons with a p_{T} greater than 25 GeV, rising to 99% above 60 GeV, as measured in $Z \to ee$ and $Z \to \mu\mu$ samples [77, 79]. Finally, the lepton tracks must point to the primary vertex of the event[3]: the longitudinal impact parameter must satisfy $|z_0| < 0.5$ mm, while the transverse impact parameter significance must satisfy $|d_0|/\sigma_{d_0} < 5$ (3) for electrons (muons).

Jets are reconstructed from three-dimensional topological energy clusters [80] in the calorimeter using the anti-k_t jet algorithm [81] with a radius parameter of 0.4. Each topological cluster is calibrated to the electromagnetic scale response prior to jet reconstruction. The reconstructed jets are then calibrated with a series of simulation-based corrections and in situ techniques based on 13 TeV data [82]. After energy calibration, jets are required to have $p_{\mathrm{T}} > 25$ GeV and $|\eta| < 2.5$. Quality criteria are imposed to identify jets arising from non-collision sources or detector noise, and any event containing such a jet is removed [83]. Finally, to reduce the effect of pile-up, an additional requirement is made using an algorithm that matches jets with $p_{\mathrm{T}} < 120$ GeV and $|\eta| < 2.4$ to tracks with $p_{\mathrm{T}} > 0.5$ GeV to identify jets consistent with originating from the primary vertex. This algorithm is known as jet vertex tagger (JVT) [84]. To identify jets containing b-hadrons, referred to as b-jets in the following, the MV2c10 tagger algorithm [85], which combines impact parameter information with the explicit identification of secondary and tertiary vertices within the jet into a multivariate discriminant, is used. Jets are b-tagged by requiring the discriminant output to be above a threshold, providing a specific b-jet efficiency in simulated $t\bar{t}$ events. A criterion with an efficiency of 70% is used to determine the b-jet multiplicity in this analysis. For this working point and for the same $t\bar{t}$ sample, the c-jet and light-jet rejection factors are 8.9 and 300, respectively [86].

To avoid counting a single detector signal as more than one lepton or jet, an overlap removal procedure is applied. First, the closest jet within $\Delta R_y = \sqrt{(\Delta y)^2 + (\Delta\phi)^2} = 0.2$[4] of a selected electron is removed. If the nearest jet surviving that selection is within $\Delta R_y = 0.4$ of the electron, the electron is discarded. Muons are removed if they are separated from the nearest jet by $\Delta R_y < 0.4$, which reduces the background from semi-leptonic decays of heavy-flavour hadrons. However, if this jet has fewer than three associated tracks, the muon is kept and the jet is removed instead; this avoids an inefficiency for high-energy muons undergoing significant energy loss in the calorimeter.

The missing transverse momentum, $E_{\mathrm{T}}^{\mathrm{miss}}$, in the event is computed as the magnitude of the negative vector sum of the p_{T} of all the selected electrons, muons and jets described above, with a correction for "soft"

[3] Events are required to have at least one reconstructed vertex with three or more associated tracks which have $p_{\mathrm{T}} > 400$ MeV. The primary vertex is chosen as the vertex candidate with the largest sum of the squared transverse momentum of associated tracks.

[4] The rapidity is defined as $y = \frac{1}{2} \ln \frac{E+p_z}{E-p_z}$, where E is the energy and p_z is the component of the momentum along the beam pipe.

energy in the event not associated with any of the hard objects. This additional term is calculated from ID tracks matched to the primary vertex to make it resilient to pile-up contamination [87]. The missing transverse momentum is not used in the event selection, but included in the multivariate discriminant used in the analysis.

Events are required to have exactly one electron or muon, with $p_{\mathrm{T}} > 27$ GeV, within $\Delta R < 0.15$ of a lepton of the same flavour reconstructed by the trigger algorithm, and at least five jets, at least two of which must be b-tagged. The total event acceptance for the H^+ signal samples ranges from 2% (at 200 GeV) to 8.5% (at 1000 GeV). After 1000 GeV, the acceptance decreases due to the boosted topology of the events, which fail the requirement on jet multiplicity. At 2000 GeV, the acceptance is only 6%. The selected events are categorised into four separate regions according to the number of reconstructed jets (j) and b-jets (b) in the event, in order to improve the sensitivity of the fit and constrain some of the systematic uncertainties. The analysis regions are 5j3b, 5j≥4b, ≥6j3b and ≥6j≥4b, where XjYb means that X jets are found in the event, and among them Y are b-tagged. The ≥5j2b region is used to derive data-based corrections, which are implemented to improve the agreement of the simulation with data.

4 Background modelling

With the isolation criteria applied both at the trigger and analysis level, as well as the purity-enhancing identification criteria used for electrons and muons (see Section 3), the background due to non-prompt leptons is expected to be negligible. To ensure that the difference between the data and the total MC prediction is not due to the existence of unaccounted non-prompt lepton background but to mismodelling of the simulation, the ratio $(N_{\mathrm{data}} - N_{\mathrm{total\,MC}})/N_{\mathrm{total\,MC}}$ was checked to not decrease when moving from a loose to a tight isolation selection. This is expected given that the MC simulates only prompt lepton background and it is unlikely for the non-prompt leptons in data to be isolated. In a scenario with background mismodelling, tighter isolation requirements would remove events on data and MC alike. All backgrounds in this analysis are estimated using the simulation samples described in Section 2.

To define the background categories in the likelihood fit (see Section 7) the $t\bar{t}$ + jets background is categorised according to the flavour of the jets in the event. Generator-level particle jets are reconstructed from stable particles (mean lifetime $\tau > 3 \times 10^{-11}$ s) using the anti-k_t algorithm with a radius parameter R = 0.4, and are required to have $p_{\mathrm{T}} > 15$ GeV and $|\eta| < 2.5$. The flavour of a jet is determined by counting the number of b- or c-hadrons within $\Delta R = 0.4$ of the jet axis. Jets matched to one or more b-hadrons, of which at least one must have p_{T} above 5 GeV, are labelled as b-jets. c-jets are defined analogously, only considering jets not already defined as b-jets. Events that have at least one b-jet, not including heavy-flavour jets from top-quark or W-boson decays, are labelled as $t\bar{t}$+ ≥1b; those with no b-jets but at least one c-jet are labelled as $t\bar{t}$+ ≥1c. Finally, events not containing any heavy-flavour jets, aside from those from top-quark or W-boson decays, are labelled as $t\bar{t}$+ light.

After the event selection, $t\bar{t}$ + jets constitutes the main background. It is observed that the simulation of $t\bar{t}$ + jets does not properly model high jet multiplicities nor the hardness of additional jet emissions, and data-based corrections are applied to the simulation [88, 89]. Data and MC prediction are compared in a sample with at least five jets and exactly two b-tagged jets. Since the mismodelling is independent from whether the additional jets are b-tagged or not, these reweighting factors are expected to improve the agreement between data and MC in the 3b and ≥ 4b regions as well, to the point that the remaining

discrepancies would be well covered by the systematic model. The reweighting factors can be expressed as:

$$R(v) = \frac{\text{Data}(v) - \text{MC}^{\text{non}-t\bar{t}}(v)}{\text{MC}^{t\bar{t}}(v)}, \tag{1}$$

where v is the variable mismodelled by the MC simulation. In this context, $t\bar{t}$+ light, $t\bar{t}$+ $\geq 1b$ and $t\bar{t}$+ $\geq 1c$, as well as Wt single top contributions, are included in the $t\bar{t}$ sample. For the range of H^+ masses considered in this analysis and assuming the observed upper limits of the cross-section times branching ratio published in Ref. [24], signal events contribute less than 1% to the ≥5j2b region and are neglected. Weights are calculated sequentially from the number of jets (R(nJets)) first, and from the corrected $H_{\text{T}}^{\text{all}}$[5] distributions in the 5j2b, 6j2b, 7j2b and ≥8j2b regions ($R(H_{\text{T}}^{\text{all}})$) afterwards. Thus, events are weighted by the product $R(\text{nJets}) \times R(H_{\text{T}}^{\text{all}})$ depending on their jet multiplicity and $H_{\text{T}}^{\text{all}}$ value . Figure 2 shows the distributions of R(nJets) in the ≥5j2b region and $R(H_{\text{T}}^{\text{all}})$ in the 5j2b, 6j2b, 7j2b and ≥8j2b regions. Among various functions tried, a hyperbola plus a sigmoid functional form was found to be the best fit to the $H_{\text{T}}^{\text{all}}$ weight distributions.

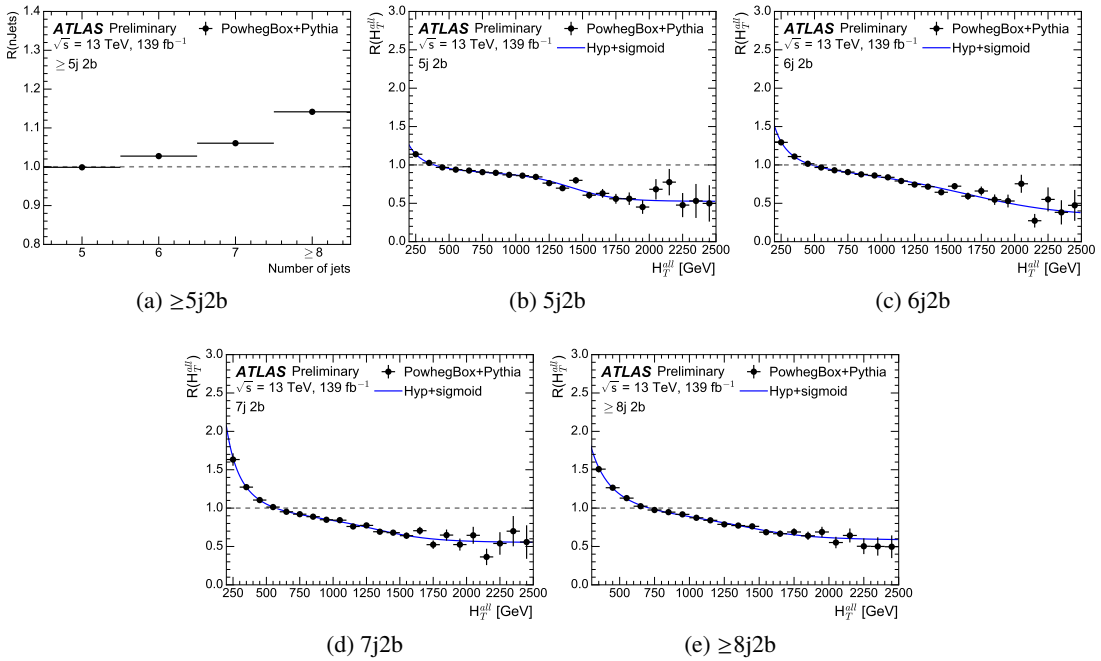

(a) ≥5j2b (b) 5j2b (c) 6j2b

(d) 7j2b (e) ≥8j2b

Figure 2: From left to right and top to bottom, distribution of the weights obtained from the comparison of the number of jets and $H_{\text{T}}^{\text{all}}$ in data and MC simulation.

After the reweighting, the agreement between simulation and data in the analysis regions improves, as can be seen, for example, in Figure 3, which shows the leading jet p_{T} distribution before the fit without and with the reweighting being applied. The $t\bar{t}$+ $\geq 1b$ and $t\bar{t}$+ $\geq 1c$ normalisation factors and their uncertainties are not applied. These normalisations are extracted from the fit to data, as shown in Section 7.

[5] $H_{\text{T}}^{\text{all}}$ is defined as the scalar sum of the transverse energy of all jets and the lepton in the event.

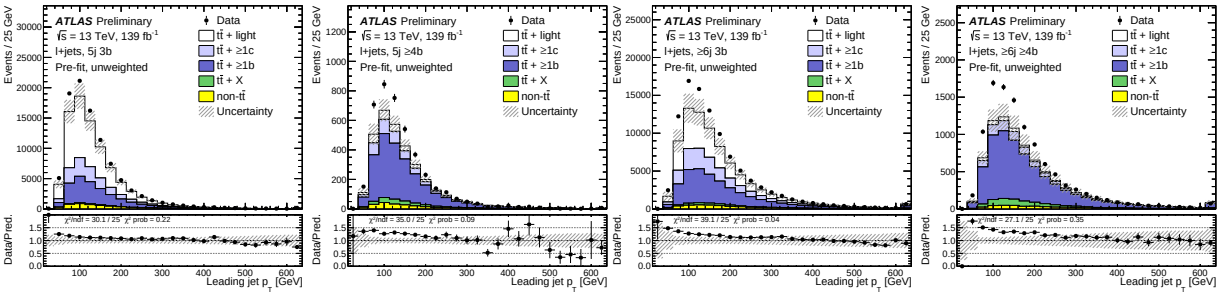

(a) 5j3b, unweighted

(b) 5j≥4b, unweighted

(c) ≥6j3b, unweighted

(d) ≥6j≥4b, unweighted

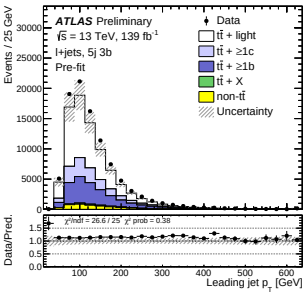

(e) 5j3b, reweighted

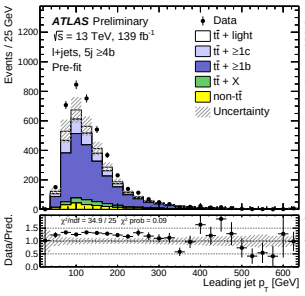

(f) 5j≥4b, reweighted

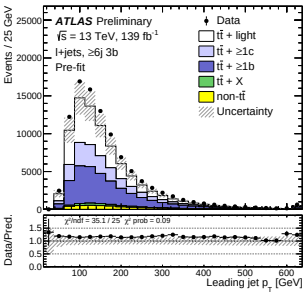

(g) ≥6j3b, reweighted

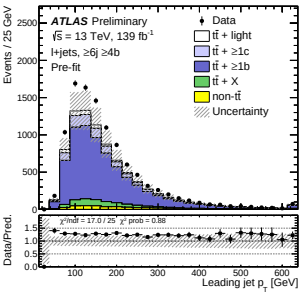

(h) ≥6j≥4b, reweighted

Figure 3: Comparison of the predicted leading jet p_{T} and data before the fit in the four analysis regions before (top) and after (bottom) the reweighting has been applied. The uncertainty bands include both statistical and systematic uncertainties. Since the normalisations of the $t\bar{t}+\geq 1b$ and $t\bar{t}+\geq 1c$ backgrounds are allowed to vary in the fit, no cross-section uncertainties associated to these processes are included. The χ^2/ndf and the χ^2 probability are shown in the bottom panels.

5 Analysis strategy

To enhance the separation between signal and background, a neural network algorithm (NN) is used. Its architecture is sequential with two fully connected layers of 64 nodes, and is implemented with the Python deep learning library, Keras [90]. The activation function used is the commonly employed "rectified linear unit (ReLu)" and the loss function is the "binary cross-entropy". Batch normalisation is performed to speed up the learning process, dropout is applied at a 10% rate, and the Adam algorithm [91] is used to optimise the parameters.

All signal samples are used in the training against all background samples, which are weighted according to their cross-sections. The training is performed separately in each analysis region, but the separate trainings include all H^+ mass samples, and use the value of the H^+ mass as a parameter [92]. For signal events the parameter corresponds to the mass of the H^+ sample they belong to, while for background events a random value of the H^+ mass, taken from the distribution of signal masses, is assigned to each event.

A total of 15 variables, described in Table 2, are used in the NN. The variables are chosen to provide the best discrimination against the $t\bar{t}+\geq 1b$ background. Among them, the kinematic discriminant, scalar sum of the p_{T} of all jets, and centrality provide the largest discrimination. The centrality is computed as the scalar sum of the p_{T} of all jets and leptons in the event divided by the sum of their energies. The kinematic discriminant is a variable reflecting the probability that an event is compatible with the $H^+ \rightarrow tb$ and the $t\bar{t}$ hypotheses, and is defined as $D = P_{H^+(\mathbf{x})}/(P_{H^+(\mathbf{x})} + P_{t\bar{t}(\mathbf{x})})$, where $P_{H^+(\mathbf{x})}$ and $P_{t\bar{t}(\mathbf{x})}$ are probability density functions for $\mathbf{x}$ under the signal hypothesis and background ($t\bar{t}$) hypothesis, respectively. The event variable $\mathbf{x}$ indicates the set of the missing transverse momentum and the four-momenta of the reconstructed lepton and the jets [24].

Table 2: List of variables included in the training of the NN.

NN variables
p_{T} of the leading jet
p_{T} of fifth leading jet
Scalar sum of the transverse p_{T} of all jets
Second Fox-Wolfram moment calculated using all jets and leptons [93]
Invariant mass of the b-jet pair with minimum ΔR
Invariant mass of the b-jet pair with maximum p_{T}
Maximal invariant mass of a b-jet pair
Invariant mass of the jet triplet with maximum p_{T}
Invariant mass of the untagged jet-pair with minimum ΔR
Average ΔR between all b-jet pairs in the event
ΔR between the lepton and the pair of b-jets with smallest ΔR
Centrality calculated using all jets and leptons
The kinematic discriminant defined in the text
Number of jets (only in ≥6j3b and ≥6j≥4b regions)
Number of b-jets (only in 5j≥4b and ≥6j≥4b regions)

Figure 4 shows the predicted NN output distributions in the four analysis regions for selected H^+ signal samples and the SM background. These distributions are used in a fit to extract the amount of H^+

signal in data. The separation of the H^+ signal from the background is most difficult for low H^+ masses because the two processes have a very similar kinematical topology. The kinematic discriminant has large separating power at low H^+ masses, whereas at higher masses, where the topologies of the H^+ signal and the background are no longer alike, other variables, like the scalar sum of the p_{T} of all jets, provide the largest separation.

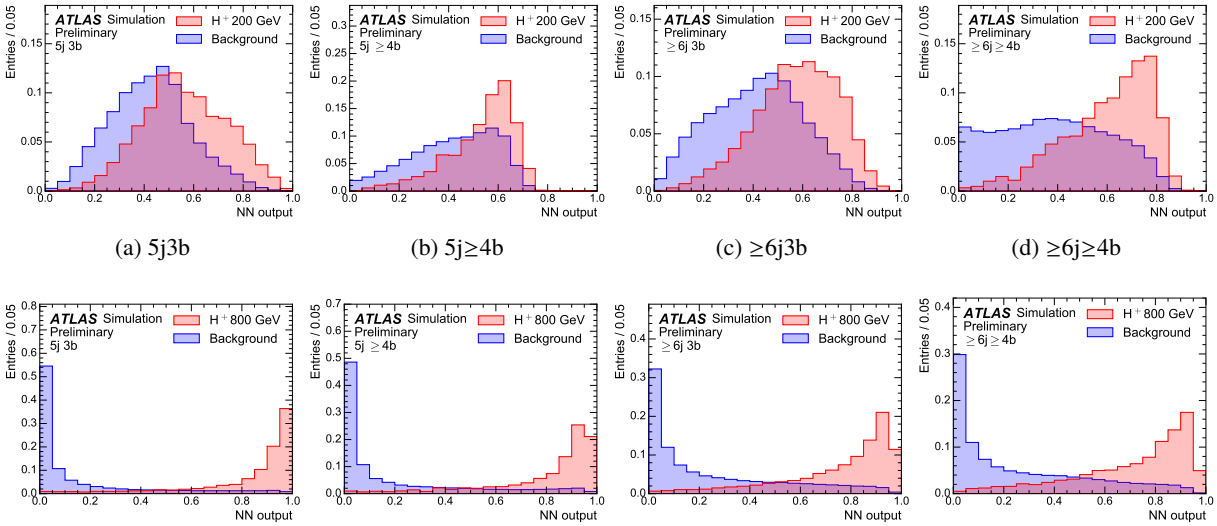

(a) 5j3b (b) 5j≥4b (c) ≥6j3b (d) ≥6j≥4b

(e) 5j3b (f) 5j≥4b (g) ≥6j3b (h) ≥6j≥4b

Figure 4: Expected output distributions of the NNs employed for H^+ masses of 200 GeV (top) and 800 GeV (bottom) for SM backgrounds and H^+ signal in the four analysis regions. All distributions are normalised to unity.

6 Systematic uncertainties

Various sources of experimental and theoretical uncertainties are considered in this analysis. They may affect the overall normalisation of the processes, the shapes of the NN distributions, or both. All the experimental uncertainties considered, with the exception of that in the luminosity, affect both normalisation and shape in all the simulated samples. Uncertainties related to the modelling of the signal and background affect both normalisation and shape, with the exception of cross-section uncertainties, which only affect the normalisation of the sample considered. Nonetheless, the normalisation uncertainties modify the relative fractions of the different samples, leading to a shape variation in the final NN output distributions. A single independent nuisance parameter (NP) is assigned to each source of systematic uncertainty in the statistical analysis. Some of the systematic uncertainties, in particular most of the experimental ones, are decomposed into several independent sources. Each individual source then has a correlated effect across all analysis regions and signal and background samples.

The uncertainty on the integrated luminosity for the full Run-2 data-set is 1.7% [94], obtained using the LUCID-2 detector [95] for the primary luminosity measurements. A variation in the pile-up reweighting of the simulated events described in Section 2 is included to cover the uncertainty in the ratio of the predicted and measured inelastic cross-sections in a given fiducial volume [96].

Uncertainties associated with charged leptons arise from the trigger selection, the object reconstruction, identification and isolation criteria, as well as the lepton momentum scale and resolution. The reconstruction, identification and isolation efficiency of electrons and muons, as well as the efficiency of the trigger used to record the events, differ slightly between data and simulation, which is compensated for by dedicated correction factors (CFs). Efficiency CFs are measured using tag-and-probe techniques on $Z \rightarrow l^+l^-$ data and simulated samples [79, 97], and are applied to the simulation to correct for the differences. The effect of these CFs, as well as of their uncertainties, are propagated as corrections to the MC event weight. Additional sources of uncertainty originate from the corrections applied to adjust the lepton momentum scale and resolution in the simulation to match those in data. These uncertainties have a small impact on the analysis.

Uncertainties associated with jets arise from the efficiency of pile-up rejection by the JVT, from the jet energy scale (JES) and resolution (JER), and from b-tagging. CFs are applied to correct for discrepancies between data and MC simulation for JVT efficiencies. These CFs are estimated using $Z(\rightarrow \mu^+\mu^-)$ + jets with tag-and-probe techniques similar to those in Ref. [84]. The JES and its uncertainty are derived by combining information from test-beam data, LHC collision data and simulation [82]. Additional uncertainties are considered, related to jet flavour, quark/gluon fraction, pile-up corrections, η dependence, high-p_{T} jets, and differences between full and fast simulation. The JER was measured in data collected in 2015-2018 and in simulation as a function of jet p_{T} and rapidity in dijet events, using a similar method to that in Ref. [98]. The uncertainty is propagated by smearing the jet p_{T} in MC. The b-tagging efficiencies in simulated samples are corrected to match efficiencies in data. CFs are derived as a function of p_{T} for b-, c- and light-jets separately in dedicated calibration analyses. For b-jet efficiencies, $t\bar{t}$ events in the di-lepton topology are used, exploiting the very pure sample of b-jets arising from the decays of the top-quarks [86]. For c-jet mistag rates, $t\bar{t}$ events in single-lepton topology are used, exploiting the c-jets from the hadronically decaying W bosons, using techniques similar to those in Ref. [99]. For light-jet mistag rates, the so-called negative-tag method similar to that in Ref. [100] is used, but using Z+jets events instead of di-jet events.

All the uncertainties described above on energy scales or resolutions of the reconstructed objects are propagated to the missing transverse momentum. Additional uncertainties in the scale and resolution of the soft term are considered, which account for the disagreement between data and MC of the p_{T} balance between the hard and the soft components. A total of three independent sources are added: an offset along the hard component p_{T} axis, and the smearing resolution along and perpendicular to this axis [101, 102]. Since the missing transverse momentum is not used in selection but only in the event reconstruction, the associated uncertainties have a small impact on the analysis.

The uncertainty in the H^+ signal due to different scale choices is estimated by varying μ_f and μ_r up and down by a factor of two. The uncertainties from the modelling of the PDF are evaluated replacing the nominal NNPDF2.3NLO PDF set by a symmetrised Hessian set, PDF4LHC15_nlo_30, following the PDF4LHC recommendations for LHC Run 2 [103].

The modelling of the $t\bar{t}$ + jets background is one of the largest sources of uncertainty in the analysis, and several different components are considered. The 6% uncertainty for the inclusive $t\bar{t}$ production cross-section predicted at NNLO+NNLL includes effects from varying μ_f and μ_r, the PDFs, α_{S}, and the top-quark mass [104]. This uncertainty is applied to $t\bar{t}$ + light only, since the normalisation of $t\bar{t}$+ $\geq 1b$ and $t\bar{t}$+ $\geq 1c$ are allowed to vary freely in the fit. Besides normalisation, the $t\bar{t}$+ light, $t\bar{t}$+ $\geq 1b$ and $t\bar{t}$+ $\geq 1c$ processes are affected by different types of uncertainties: the uncertainties associated with additional Feynman diagrams for the $t\bar{t}$+ light are constrained from relatively precise measurements in data; $t\bar{t}$+ $\geq 1b$ and $t\bar{t}$+ $\geq 1c$ can have similar or different Feynman diagrams depending on the flavour scheme used for

the PDF, and the different masses of the b- and the c-quarks contribute to additional differences between these two processes. For these reasons, all uncertainties in the $t\bar{t}$ + jets background modelling are assigned independent NP for $t\bar{t}$+ light, $t\bar{t}$+ $\geq 1b$ and $t\bar{t}$+ $\geq 1c$. Systematic uncertainties on the acceptance and shapes are extracted by comparing the nominal prediction to alternative MC samples or settings. Such comparisons would significantly change the fractions of $t\bar{t}$+ $\geq 1b$ and $t\bar{t}$+ $\geq 1c$. However, since the normalisation of these sub-processes in the analysis regions is measured in the fit, these alternative predictions are reweighted in such a way that they keep the same fractions of $t\bar{t}$+ $\geq 1b$ and $t\bar{t}$+ $\geq 1c$ as the nominal sample in the phase-space selected by the analysis.

The uncertainty due to initial state radiation (ISR) is estimated by scaling μ_f and μ_r up and down by a factor of two, and by using the *Var3cUp* (*Var3cDown*) variation from the A14 tune [46], corresponding to $\alpha_S^{\text{ISR}} = 0.140$ (0.115) instead of the nominal $\alpha_S^{\text{ISR}} = 0.127$. For the final state radiation (FSR), the amount of radiation is increased (decreased) by varying μ_r for QCD emission by a factor of 0.5 (2.0), corresponding to $\alpha_S^{\text{FSR}} = 0.1423$ (0.1147) instead of the nominal $\alpha_S^{\text{FSR}} = 0.127$. The nominal PowhegBox+Pythia sample is compared to the PowhegBox+Herwig sample to assess the effect of the PS and hadronisation models, and to the MadGraph5_aMC@NLO sample to assess the effect of the NLO matching technique. Finally, the weights derived in Section 4 to improve the agreement of the simulation with data are varied within their statistical uncertainties, in a correlated way among the three $t\bar{t}$ + jets components. All the sources of systematic uncertainty for the $t\bar{t}$ + jets modelling are summarised in Table 3.

Table 3: Summary of the sources of systematic uncertainty for $t\bar{t}$ + jets modelling. The systematic uncertainties listed in the second section of the table are evaluated in such a way as to have no impact on the normalisation of the three, $t\bar{t}$+ $\geq 1b$, $t\bar{t}$+ $\geq 1c$ and $t\bar{t}$+ light, components in the phase-space selected in the analysis. The last column of the table indicates the $t\bar{t}$ + jets components to which the systematic uncertainty is assigned. All systematic uncertainty sources, except those associated to the $t\bar{t}$ reweighting, are treated as uncorrelated across the three components.

Uncertainty source	Description		Components
$t\bar{t}$ cross-section	Up or down by 6%		$t\bar{t}$+ light
$t\bar{t}$ reweighting	Statistical uncertainties of fitted function (six) parameters		All $t\bar{t}$ and Wt
$t\bar{t}$+ $\geq 1b$ normalisation	Free-floating		$t\bar{t}$+ $\geq 1b$
$t\bar{t}$+ $\geq 1c$ normalisation	Free-floating		$t\bar{t}$+ $\geq 1c$
NLO matching	MadGraph5_aMC@NLO+Pythia	vs PowhegBox+Pythia	All $t\bar{t}$
PS & hadronisation	PowhegBox+Herwig	vs PowhegBox+Pythia	All $t\bar{t}$
α_S^{ISR}	*Var3cUp* (*Var3cDown*)	in PowhegBox+Pythia	All $t\bar{t}$
μ_f	Scaling by 0.5 (2.0)	in PowhegBox+Pythia	All $t\bar{t}$
μ_r	Scaling by 0.5 (2.0)	in PowhegBox+Pythia	All $t\bar{t}$
FSR	Varying α_S^{FSR} (PS)	in PowhegBox+Pythia	All $t\bar{t}$

A 5% uncertainty is considered for the cross-sections of the three single-top production modes [105–109]. Uncertainties associated with the PS and hadronisation model, and with the NLO matching scheme are evaluated by comparing, for each process, the nominal PowhegBox+Pythia sample to a sample produced using PowhegBox+Herwig and MadGraph5_aMC@NLO+Pythia, respectively. As mentioned in Section 4, the Wt single-top mode is included in the reweighting procedure, and thus the same uncertainties used for $t\bar{t}$ are applied here. The uncertainty associated to the interference between Wt and $t\bar{t}$ production at NLO [60] is assessed by comparing the nominal PowhegBox+Pythiasample produced using the "diagram removal" scheme to an alternative sample produced with the same generator but using the "diagram subtraction" scheme [59, 60].

The predicted SM $t\bar{t}H$ signal cross-section uncertainty is $^{+5.8\%}_{-9.2\%}$ (QCD scale) $\pm 3.6\%$ (PDF + α_S) [37, 110–114]. Uncertainties in the Higgs boson branching ratios amount to 2.2% for the $b\bar{b}$ decay mode [37]. For the ISR and FSR, the amount of radiation is varied following the same procedure as for $t\bar{t}$. The nominal PowhegBox+Pythia sample is compared to the PowhegBox+Herwig sample to assess the uncertainty due to PS and hadronisation, and to the MadGraph5_aMC@NLO sample for the uncertainty due to the NLO matching.

The uncertainty of the $t\bar{t}V$ NLO cross-section prediction is 15%, split into PDF and scale uncertainties as for $t\bar{t}H$ [37, 115]. An additional $t\bar{t}V$ modelling uncertainty, related to the choice of PS and hadronisation model and NLO matching scheme, is assessed by comparing the nominal MadGraph5_aMC@NLO+Pythia samples with alternative ones generated with Sherpa.

An overall 50% normalisation uncertainty is considered for the four-tops background, covering effects from varying μ_f, μ_r, PDFs and α_S [43, 116]. The small background tZq is assigned a 7.9% and a 0.9% accounting for μ_f and μ_r scales and PDF variations, respectively. Finally, a single 50% uncertainty is used for tZW [43].

An uncertainty of 40% is assumed for the W+jets normalisation, with an additional 30% for W + heavy-flavour jets, taken as uncorrelated between events with two and more than two heavy-flavour jets. These uncertainties are based on variations of the μ_f and μ_r and of the matching parameters in the Sherpa samples. An uncertainty of 35% is applied to the Z+jets normalisation, uncorrelated across jet bins, to account for both the variations of the scales and matching parameters in the Sherpa samples and the uncertainty in the extraction from data of the correction factor for the heavy-flavour component [51, 117]. Finally, a total 50% normalisation uncertainty in the diboson background is assumed, which includes uncertainties in the inclusive cross-section and additional jet production [118].

7 Results

A binned maximum-likelihood fit to the data is performed simultaneously to the NN output distributions in the four analysis regions, and each mass hypothesis is tested separately. The procedures used to quantify the agreement with the background-only hypothesis or background-plus-signal hypothesis and to determine exclusion limits are based on the profile likelihood ratio test and the CLs method [119–121]. The parameter of interest is the product of the production cross section $\sigma(pp \to tbH^+)$ and the branching ratio $\mathrm{BR}(H^+ \to tb)$. All systematic uncertainties are implemented as nuisance parameters with log-normal constraint terms. There are about 170 nuisance parameters considered in the fit, the number varying slightly across the range of mass hypotheses. A summary of the systematic uncertainties with similar sources grouped together is given in Table 4. Depending on the particular H^+ mass hypothesis, the total systematic uncertainty is dominated by the uncertainties in the modelling of the $t\bar{t}$ background, in particular $t\bar{t}+\geq 1b$ and $t\bar{t}+\geq 1c$, jet flavour-tagging uncertainties, and jet energy scale and resolution.

Table 5 shows the event yields after the background-plus-signal fit under the 200 GeV and 800 GeV H^+ mass hypotheses. Values not significantly different from zero, $\sigma(tbH^+) \times \mathrm{BR}(H^+ \to tb) = 1.12$ pb and $\sigma(tbH^+) \times \mathrm{BR}(H^+ \to tb) = 0.022$ pb, are obtained from the fit in each case. The corresponding post-fit distributions of the NN output in each analysis region are shown in Figure 5 for the 200 GeV and 800 GeV H^+ mass hypotheses.

The 95% confidence level (CL) upper limits on $\sigma(pp \to tbH^+) \times \mathrm{BR}(H^+ \to tb)$ using the CLs method are presented in Figure 6. Uncertainties in the predicted H^+ cross-sections or branching ratios are not

Table 4: Summary of the effects of the statistical and systematic uncertainties on $\mu = \sigma(pp \to tbH^+) \times \mathrm{BR}(H^+ \to tb)$ is shown for an H^+ signal with a mass of 200 and 800 GeV. Due to correlations between the different sources of uncertainty, the total systematic uncertainty can be different from the sum in quadrature of the individual sources. The normalisation factors for both $t\bar{t}+\geq 1b$ and $t\bar{t}+\geq 1c$ are included in the statistical component.

Uncertainty Source	$\Delta\mu(H^+_{200})$ [pb]	$\Delta\mu(H^+_{800})$ [pb]
$t\bar{t}+\geq 1b$ modelling	0.94	0.025
Jet energy scale and resolution	0.38	0.0095
$t\bar{t}+\geq 1c$ modelling	0.32	0.006
Jet flavour tagging	0.24	0.025
Reweighting	0.22	0.007
$t\bar{t}+$ light modelling	0.23	0.009
Other background modelling	0.15	0.011
MC statistics	0.11	0.008
JVT, pile-up modelling	0.05	0.002
Luminosity	<0.01	0.002
Lepton ID, isolation, trigger, $E_{\mathrm{T}}^{\mathrm{miss}}$	<0.01	<0.001
H^+ modelling	0.04	0.002
Total systematic uncertainty	1.35	0.05
$t\bar{t}+\geq 1b$ normalisation	0.28	0.008
$t\bar{t}+\geq 1c$ normalisation	0.023	0.016
Total statistical uncertainty	0.42	0.025
Total uncertainty	1.36	0.054

included. The observed (expected) limits range from $\sigma \times \mathrm{BR} = 3.6\,(2.6)$ pb at $m_{H^+} = 200$ GeV to $\sigma \times \mathrm{BR} = 0.035\,(0.019)$ pb at $m_{H^+} = 2$ TeV.

Figure 7 shows 95% CL exclusion limits set on $\tan\beta$ for various benchmark scenarios in the MSSM. In the hMSSM framework, effective couplings of the lighter Higgs boson to the top-quark, bottom-quark and vector bosons are derived from fits to LHC data on the production and decay rates of the observed Higgs boson, including the limits from the negative search of heavier neutral and charged Higgs boson states. The M_h^{125}, $M_h^{125}(\tilde{\chi})$ and $M_h^{125}(\tilde{\tau})$ scenarios also feature a scalar with mass and couplings compatible with those of the observed Higgs boson, and force a significant portion of their parameter space to be compatible with the limits from the SUSY searches. In the M_h^{125} scenario all supersymmetric particles are relatively heavy and the decays of the MSSM Higgs bosons are essentially unaffected, whereas the other two models include either light charginos and neutralinos ($M_h^{125}(\tilde{\chi})$) or light staus ($M_h^{125}(\tilde{\tau})$). In both cases a charged Higgs of sufficient high mass is allowed to decay to the supersymmetric particles. Uncertainties in the predicted H^+ cross-sections or branching ratios are not included in the limits. For all scenarios except the hMSSM, Higgs masses and mixing (and effective Yukawa couplings) have been calculated with the code Feynhiggs [122–128]. Whereas in the hMSSM branching ratios are solely computed with HDECAY [129, 130], all other scenarios combine the most precise results of FeynHiggs, HDECAY and PROPHECY4f [131, 132].

In the context of these scenarios, $\tan\beta$ values below 1 are observed to be excluded at 95% CL for H^+ masses between 200 and ~790 GeV. High values of $\tan\beta$ between 34 and 60 are excluded in a similar

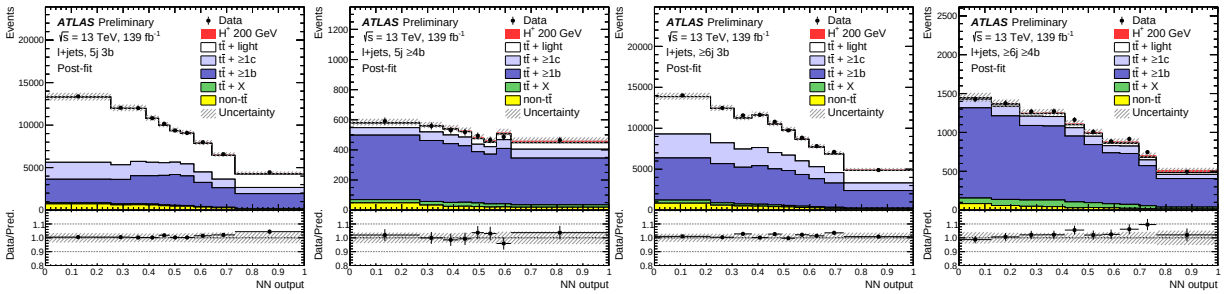

(a) 5j3b (b) 5j≥4b (c) ≥ 6j3b (d) ≥6j≥4b

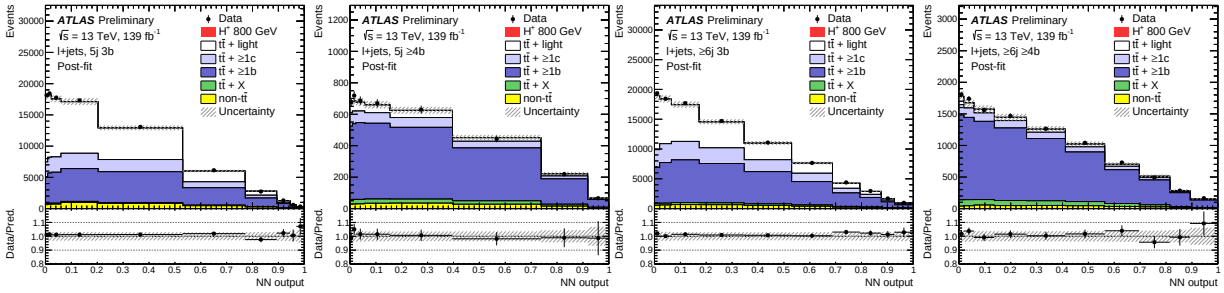

(e) 5j3b (f) 5j≥4b (g) ≥ 6j3b (h) ≥6j≥4b

Figure 5: Distributions of the NN output after the fit for the 200 GeV (top) and 800 GeV (bottom) H^+ mass hypotheses in the four analysis regions.

mass range in the hMSSM and $M_h^{125}(\tilde{\chi})$ models. The most stringent exclusion limit of $\tan\beta$ of 2 is set for the H^+ mass hypothesis of 225 GeV in the hMSSM and $M_h^{125}(\tilde{\chi})$ models and for the 300 GeV H^+ mass hypothesis in the M_h^{125} and $M_h^{125}(\tilde{\tau})$ models.

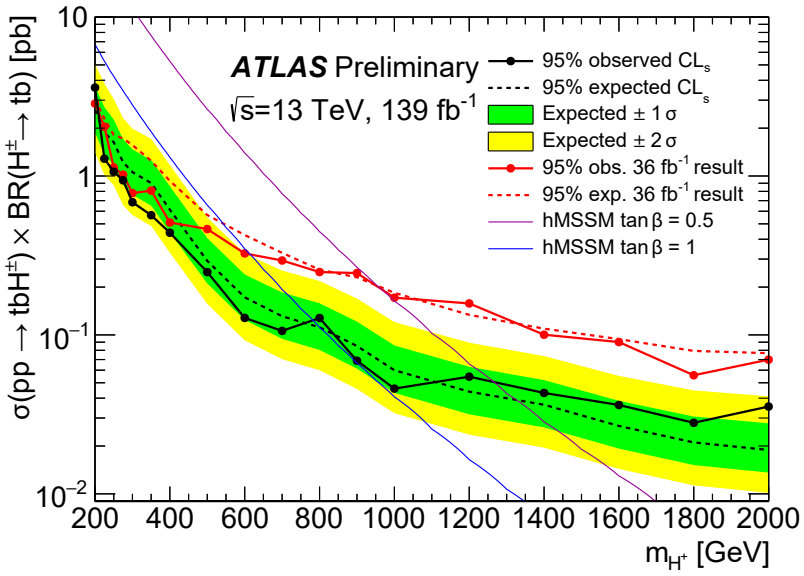

Figure 6: Expected and observed limits for the production of $H^+ \to tb$ in association with a top-quark and a bottom-quark. The bands surrounding the expected limit show the 68% and 95% confidence intervals. The red lines show the expected and observed 95% CL exclusion limits obtained with the 36 fb^{-1} data sample [24]. Theory predictions are shown for two representative values of $\tan\beta$ in the hMSSM benchmark scenario. Uncertainties in the predicted H^+ cross-sections or branching ratios are not considered.

Table 5: Event yields of the H^+ signal and SM background processes in the four analysis regions after the fit to the data under the H^+ mass hypotheses of 200 GeV (top) and 800 GeV (bottom). The quoted uncertainties take into account correlations and constraints of the nuisance parameters, and include both statistical and systematic uncertainties. The signal yield uncertainty includes the uncertainty on the signal strength fitted under the 200 or 800 GeV H^+ mass hypotheses.

m_{H^+}= 200 GeV hypothesis				
	5j, 3b	5j, ≥ 4b	≥ 6j, 3b	≥ 6j, ≥ 4b
$t\bar{t}$+ light	45000 ± 4000	300 ± 110	32000 ± 4000	340 ± 140
$t\bar{t}$+ ≥1b	29700 ± 2800	2950 ± 220	40200 ± 3300	7900 ± 500
$t\bar{t}$+ ≥1c	14000 ± 4000	440 ± 140	19000 ± 5000	1000 ± 290
$t\bar{t}$ + W	110 ± 15	3.2 ± 0.6	237 ± 35	16.3 ± 2.7
$t\bar{t}$ + Z	300 ± 40	50 ± 6	670 ± 90	174 ± 23
Single top Wt-channel	2300 ± 600	80 ± 50	1900 ± 800	150 ± 90
Single top t- channel	740 ± 300	51 ± 20	500 ± 400	60 ± 50
Other top sources	128 ± 16	17.5 ± 3.2	180 ± 70	58 ± 24
VV & V + jets	1600 ± 600	64 ± 23	1500 ± 600	110 ± 40
$t\bar{t}H$	530 ± 60	127 ± 19	1140 ± 120	430 ± 60
H^+	700 ± 900	70 ± 90	800 ± 900	180 ± 220
Total	95700 ± 2900	4150 ± 140	98300 ± 2900	10500 ± 400
Data	95852	4109	98929	10552

m_{H^+}= 800 GeV hypothesis				
	5j, 3b	5j, ≥ 4b	≥ 6j, 3b	≥ 6j, ≥ 4b
$t\bar{t}$+ light	46000 ± 4000	330 ± 120	33000 ± 4000	500 ± 200
$t\bar{t}$+ ≥1b	29600 ± 3100	2920 ± 210	41000 ± 4000	8100 ± 400
$t\bar{t}$+ ≥1c	14000 ± 6000	440 ± 190	17000 ± 7000	870 ± 330
$t\bar{t}$ + W	108 ± 15	3.3 ± 0.6	233 ± 35	16.0 ± 2.7
$t\bar{t}$ + Z	300 ± 40	50 ± 7	660 ± 90	171 ± 23
Single top Wt-channel	2000 ± 500	56 ± 33	1400 ± 500	100 ± 60
Single top t-channel	740 ± 300	53 ± 21	600 ± 500	70 ± 50
Other top sources	130 ± 16	17.7 ± 3.2	190 ± 70	61 ± 24
VV & V + jets	1900 ± 700	73 ± 25	1700 ± 600	130 ± 50
$t\bar{t}H$	520 ± 60	125 ± 19	1130 ± 120	420 ± 60
H^+	30 ± 80	4 ± 10	70 ± 180	20 ± 50
Total	94700 ± 2800	4070 ± 140	97900 ± 2800	10400 ± 400
Data	95852	4109	98929	10552

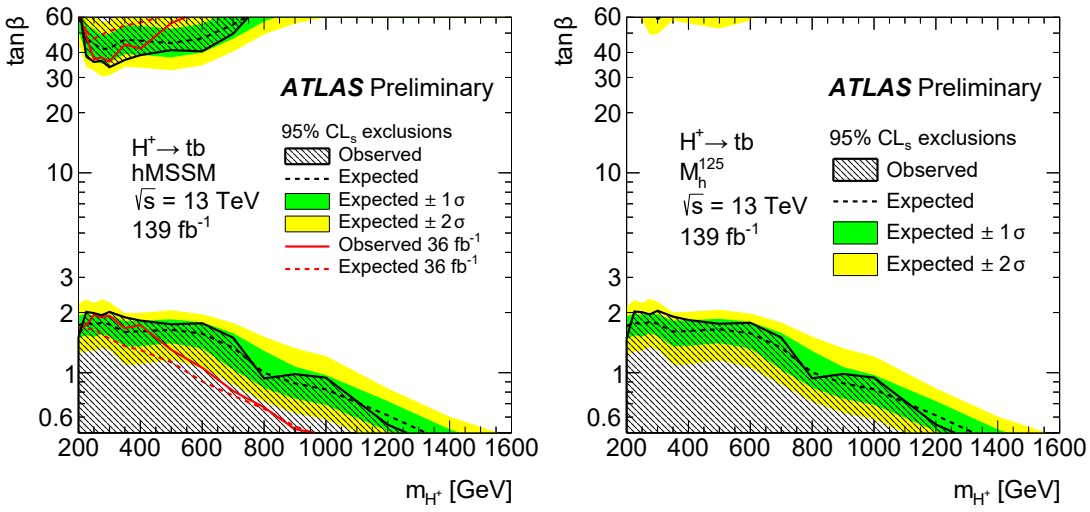

(a) hMSSM

(b) M_h^{125}

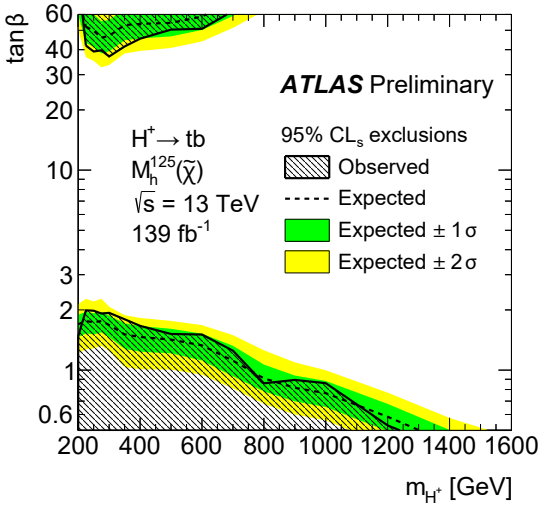

(c) $M_h^{125}(\tilde{\chi})$

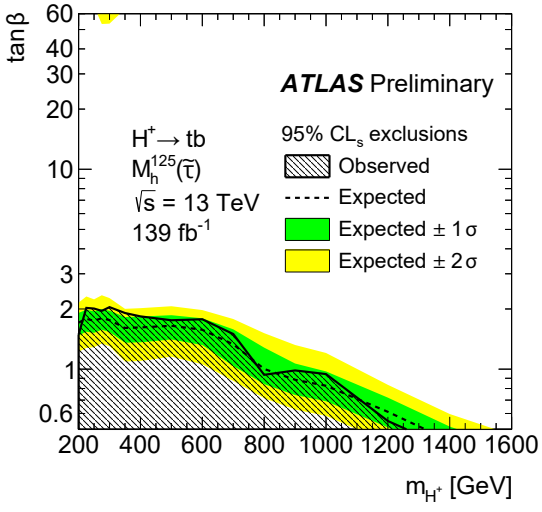

(d) $M_h^{125}(\tilde{\tau})$

Figure 7: Expected and observed limits on $\tan\beta$ as a function of m_{H^+} in the hMSSM scenario and various M_h^{125} scenarios. Limits are shown for $\tan\beta$ values in the range of 0.5–60, where predictions are available in all scenarios. The bands surrounding the expected limits show the 68% and 95% confidence intervals. Uncertainties in the predicted H^+ cross-sections or branching ratios are not considered.

8 Conclusion

A search for charged Higgs bosons is presented using a data sample corresponding to an integrated luminosity of 139 fb^{-1} from pp collisions at $\sqrt{s}$ = 13 TeV, recorded with the ATLAS detector at the LHC. The search for $pp \to tbH^+$ is performed in the H^+ mass range 200–2000 GeV. A neural network which combines several kinematic variables is built in the regions where the signal rate is expected to be largest. The NN is parametrised as a function of the H^+ mass, and a fit to the data is performed simultaneously to the NN output distributions in the analysis regions, separately for each signal mass hypothesis.

No significant excess above the expected SM background is found and observed (expected) 95% CL upper limits are set on the $\sigma(pp \to tbH^+)$ production cross-section times the branching ratio BR($H^+ \to tb$), which range from $\sigma \times$ BR = 3.6 (2.6) pb at m_{H^+}= 200 GeV to $\sigma \times$ BR = 0.035 (0.019) pb at m_{H^+} = 2 TeV. In comparison with the previous ATLAS search for tbH^+ production followed by $H^+ \to tb$ decays with 36 fb^{-1}, the observed $\sigma \times$ BR limits improved by 6-70%, depending on the H^+ mass.

In the context of the hMSSM and several M_h^{125} scenarios, some values of $\tan\beta$, in the range 0.5–2, are excluded for H^+ masses between 200 and 1200 GeV. For H^+ masses between ~200 and ~750 GeV, high values of $\tan\beta$ up to 60 are also excluded.

Appendix

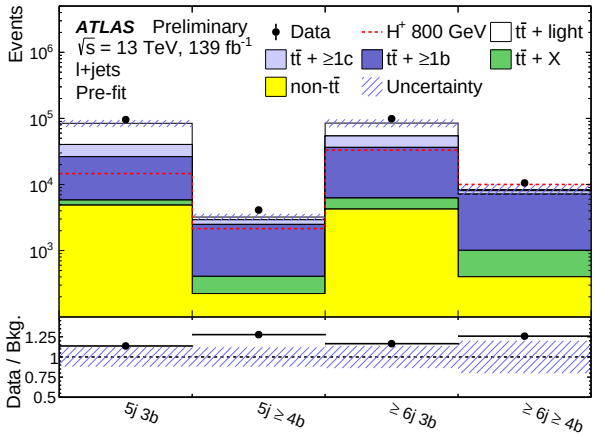

Figure 8: Comparison of predicted and observed event yields. Only background processes are considered and are normalised according to their cross-section. The prediction has not been fitted to the data. Yields of a charged Higgs boson with a mass of 800 GeV corresponding to a cross-section of 10 pb are overlaid in red. The lower panel displays the ratio of the data to the total background. The hatched bands show uncertainties before the fit to the data.

References

[1] ATLAS Collaboration, *Observation of a new particle in the search for the Standard Model Higgs boson with the ATLAS detector at the LHC*, Phys. Lett. B **716** (2012) 1, arXiv: 1207.7214 [hep-ex] (cit. on p. 2).

[2] CMS Collaboration, *Observation of a new boson at a mass of 125 GeV with the CMS experiment at the LHC*, Phys. Lett. B **716** (2012) 30, arXiv: 1207.7235 [hep-ex] (cit. on p. 2).

[3] ATLAS and CMS Collaborations, *Combined measurement of the Higgs boson mass in pp collisions at $\sqrt{s} = 7$ and 8 TeV with the ATLAS and CMS experiments*, Phys. Rev. Lett. **114** (2015) 191803, arXiv: 1503.07589 [hep-ex] (cit. on p. 2).

[4] T. D. Lee, *A Theory of Spontaneous T Violation*, Phys. Rev. D **8** (1973) 1226 (cit. on p. 2).

[5] G. Branco, P. Ferreira, L. Lavoura, M. Rebelo, M. Sher et al., *Theory and phenomenology of two-Higgs-doublet models*, Phys.Rept. **516** (2012) 1, arXiv: 1106.0034 [hep-ph] (cit. on p. 2).

[6] K. Inoue, A. Kakuto, H. Komatsu and S. Takeshita, *Aspects of Grand Unified Models with Softly Broken Supersymmetry*, Prog.Theor.Phys. **68** (1982) 927 (cit. on p. 2).

[7] T. Cheng and L.-F. Li, *Neutrino Masses, Mixings and Oscillations in SU(2) x U(1) Models of Electroweak Interactions*, Phys. Rev. **D22** (1980) 2860 (cit. on p. 2).

[8] T. P. Cheng and L.-F. Li, *Neutrino Masses, Mixings and Oscillations in SU(2)×U(1) Models of Electroweak Interactions*, Phys. Rev. D **22** (1980) 2860 (cit. on p. 2).

[9] J. Schechter and J. W. F. Valle, *Neutrino Masses in SU(2)×U(1) Theories*, Phys. Rev. D **22** (1980) 2227 (cit. on p. 2).

[10] G. Lazarides, Q. Shafi and C. Wetterich, *Proton Lifetime and Fermion Masses in an SO(10) Model*, Nucl. Phys. B **181** (1981) 287 (cit. on p. 2).

[11] R. N. Mohapatra and G. Senjanovic, *Neutrino Masses and Mixings in Gauge Models with Spontaneous Parity Violation*, Phys. Rev. D **23** (1981) 165 (cit. on p. 2).

[12] M. Magg and C. Wetterich, *Neutrino Mass Problem and Gauge Hierarchy*, Phys. Lett. B **94** (1980) 61 (cit. on p. 2).

[13] ATLAS Collaboration, *Search for charged Higgs bosons decaying via $H^{\pm} \to \tau\nu$ in $t\bar{t}$ events using pp collision data at $\sqrt{s} = 7$ TeV with the ATLAS detector*, JHEP **06** (2012) 039, arXiv: 1204.2760 [hep-ex] (cit. on p. 2).

[14] ATLAS Collaboration, *Search for charged Higgs bosons through the violation of lepton universality in $t\bar{t}$ events using pp collision data at $\sqrt{s} = 7$ TeV with the ATLAS experiment*, JHEP **03** (2013) 076, arXiv: 1212.3572 [hep-ex] (cit. on p. 2).

[15] ATLAS Collaboration, *Search for charged Higgs bosons decaying via $H^{\pm} \to \tau^{\pm}\nu$ in fully hadronic final states using pp collision data at $\sqrt{s} = 8$ TeV with the ATLAS detector*, JHEP **03** (2015) 088, arXiv: 1412.6663 [hep-ex] (cit. on p. 2).

[16] CMS Collaboration, *Search for a light charged Higgs boson in top quark decays in pp collisions at $\sqrt{s} = 7$ TeV*, JHEP **07** (2012) 143, arXiv: 1205.5736 [hep-ex] (cit. on p. 2).

[17] CMS Collaboration, *Search for a charged Higgs boson in pp collisions at $\sqrt{s} = 8$ TeV*, JHEP **11** (2015) 018, arXiv: 1508.07774 [hep-ex] (cit. on p. 2).

[18] ATLAS Collaboration, *Search for charged Higgs bosons decaying via $H^{\pm} \to \tau^{\pm}\nu_{\tau}$ in the τ+jets and τ+lepton final states with 36 fb^{-1} of pp collision data recorded at $\sqrt{s} = 13$ TeV with the ATLAS experiment*, JHEP **09** (2018) 139, arXiv: 1807.07915 [hep-ex] (cit. on p. 2).

[19] ATLAS Collaboration, *Search for a light charged Higgs boson in the decay channel $H^{+} \to c\bar{s}$ in $t\bar{t}$ events using pp collisions at $\sqrt{s} = 7$ TeV with the ATLAS detector*, Eur. Phys. J. C **73** (2013) 2465, arXiv: 1302.3694 [hep-ex] (cit. on p. 2).

[20] CMS Collaboration, *Search for a light charged Higgs boson decaying to $c\bar{s}$ in pp collisions at $\sqrt{s} = 8$ TeV*, JHEP **12** (2015) 178, arXiv: 1510.04252 [hep-ex] (cit. on p. 2).

[21] CMS Collaboration, *Search for a charged Higgs boson decaying to charm and bottom quarks in proton–proton collisions at $\sqrt{s} = 8$ TeV*, JHEP **11** (2018) 115, arXiv: 1808.06575 [hep-ex] (cit. on p. 2).

[22] ATLAS Collaboration, *Search for charged Higgs bosons in the $H^{\pm} \to tb$ decay channel in pp collisions at $\sqrt{s} = 8$ TeV using the ATLAS detector*, JHEP **03** (2016) 127, arXiv: 1512.03704 [hep-ex] (cit. on p. 2).

[23] ATLAS Collaboration, *Search for charged Higgs bosons produced in association with a top quark and decaying via $H^{\pm} \to \tau\nu$ using pp collision data recorded at $\sqrt{s} = 13$ TeV by the ATLAS detector*, Phys. Lett. B **759** (2016) 555, arXiv: 1603.09203 [hep-ex] (cit. on p. 2).

[24] ATLAS Collaboration, *Search for charged Higgs bosons decaying into top and bottom quarks at $\sqrt{s} = 13$ TeV with the ATLAS detector*, JHEP **11** (2018) 085, arXiv: 1808.03599 [hep-ex] (cit. on pp. 2, 8, 10, 17).

[25] CMS Collaboration, *Search for a charged Higgs boson decaying into top and bottom quarks in events with electrons or muons in proton–proton collisions at $\sqrt{s} = 13$ TeV*, JHEP **01** (2020) 096, arXiv: 1908.09206 [hep-ex] (cit. on p. 2).

[26] CMS Collaboration, *Search for charged Higgs bosons decaying into a top and a bottom quark in the all-jet final state of pp collisions at $\sqrt{s} = 13$ TeV*, (2020), arXiv: 2001.07763 [hep-ex] (cit. on p. 2).

[27] ATLAS Collaboration, *Search for a Charged Higgs Boson Produced in the Vector-Boson Fusion Mode with Decay $H^{\pm} \to W^{\pm}Z$ using pp Collisions at $\sqrt{s} = 8$ TeV with the ATLAS Experiment*, Phys. Rev. Lett. **114** (2015) 231801, arXiv: 1503.04233 [hep-ex] (cit. on p. 2).

[28] CMS Collaboration, *Search for charged Higgs bosons produced via vector boson fusion and decaying into a pair of W and Z bosons using pp collisions at $\sqrt{s} = 13$ TeV*, Phys. Rev. Lett. **119** (2017) 141802, arXiv: 1705.02942 [hep-ex] (cit. on p. 2).

[29] ATLAS Collaboration, *Search for dijet resonances in events with an isolated charged lepton using $\sqrt{s} = 13$ TeV proton–proton collision data collected by the ATLAS detector*, Journal of High Energy Physics **2020** (2020), arXiv: 2002.11325 [hep-ex] (cit. on p. 2).

[30] A. Djouadi and J. Quevillon, *The MSSM Higgs sector at a high M_{SUSY}: reopening the low tanβ regime and heavy Higgs searches*, JHEP **10** (2013) 028, arXiv: 1304.1787 [hep-ph] (cit. on p. 2).

[31] L. Maiani, A. Polosa and V. Riquer, *Bounds to the Higgs Sector Masses in Minimal Supersymmetry from LHC Data*, Phys. Lett. B **724** (2013) 274, arXiv: 1305.2172 [hep-ph] (cit. on p. 2).

[32] A. Djouadi et al., *The post-Higgs MSSM scenario: Habemus MSSM?*, Eur. Phys. J. C **73** (2013) 2650, arXiv: 1307.5205 [hep-ph] (cit. on p. 2).

[33] A. Djouadi, L. Maiani, A. Polosa, J. Quevillon and V. Riquer, *Fully covering the MSSM Higgs sector at the LHC*, JHEP **06** (2015) 168, arXiv: 1502.05653 [hep-ph] (cit. on p. 2).

[34] E. Bagnaschi et al., *MSSM Higgs boson searches at the LHC: benchmark scenarios for Run 2 and beyond*, Eur. Phys. J. C **79** (2019), URL: http://dx.doi.org/10.1140/epjc/s10052-019-7114-8 (cit. on p. 2).

[35] C. Degrande, M. Ubiali, M. Wiesemann and M. Zaro, *Heavy charged Higgs boson production at the LHC*, JHEP **10** (2015) 145, arXiv: 1507.02549 [hep-ph] (cit. on pp. 2, 3).

[36] M. Flechl, R. Klees, M. Krämer, M. Spira and M. Ubiali, *Improved cross-section predictions for heavy charged Higgs boson production at the LHC*, Physical Review D **91** (2015), ISSN: 1550-2368, URL: http://dx.doi.org/10.1103/PhysRevD.91.075015 (cit. on p. 2).

[37] D. de Florian et al., *Handbook of LHC Higgs Cross Sections: 4. Deciphering the Nature of the Higgs Sector*, (2016), arXiv: 1610.07922 [hep-ph] (cit. on pp. 2, 14).

[38] S. Dittmaier, M. Krämer, M. Spira and M. Walser, *Charged-Higgs-boson production at the LHC: Next-to-leading-order supersymmetric QCD corrections*, Physical Review D **83** (2011), ISSN: 1550-2368, URL: http://dx.doi.org/10.1103/PhysRevD.83.055005 (cit. on p. 2).

[39] E. L. Berger, T. Han, J. Jiang and T. Plehn, *Associated production of a top quark and a charged Higgs boson*, Physical Review D **71** (2005), ISSN: 1550-2368, URL: http://dx.doi.org/10.1103/PhysRevD.71.115012 (cit. on p. 2).

[40] ATLAS Collaboration, *The ATLAS Experiment at the CERN Large Hadron Collider*, JINST **3** (2008) S08003 (cit. on p. 3).

[41] ATLAS Collaboration, *Performance of the ATLAS trigger system in 2015*, Eur. Phys. J. C **77** (2017) 317, arXiv: 1611.09661 [hep-ex] (cit. on p. 3).

[42] ATLAS Collaboration, *Performance of electron and photon triggers in ATLAS during LHC Run 2*, Eur. Phys. J. C **80** (2020), arXiv: 1909.00761 [hep-ex] (cit. on p. 3).

[43] J. Alwall et al., *The automated computation of tree-level and next-to-leading order differential cross sections, and their matching to parton shower simulations*, JHEP **07** (2014) 079, arXiv: 1405.0301 [hep-ph] (cit. on pp. 3, 14).

[44] R. D. Ball et al., *Parton distributions with LHC data*, Nucl. Phys. B **867** (2013) 244, arXiv: 1207.1303 [hep-ph] (cit. on p. 3).

[45] T. Sjöstrand, S. Mrenna and P. Z. Skands, *A brief introduction to PYTHIA 8.1*, Comput. Phys. Commun. **178** (2008) 852, arXiv: 0710.3820 [hep-ph] (cit. on p. 3).

[46] ATLAS Collaboration, *ATLAS Pythia 8 tunes to 7 TeV data*, ATL-PHYS-PUB-2014-021, 2014, URL: https://cds.cern.ch/record/1966419 (cit. on pp. 3, 13).

[47] P. Nason, *A new method for combining NLO QCD with shower Monte Carlo algorithms*, JHEP **11** (2004) 040, arXiv: hep-ph/0409146 (cit. on p. 4).

[48] S. Frixione, P. Nason and C. Oleari, *Matching NLO QCD computations with parton shower simulations: the POWHEG method*, JHEP **11** (2007) 070, arXiv: 0709.2092 [hep-ph] (cit. on p. 4).

[49] S. Alioli, P. Nason, C. Oleari and E. Re, *A general framework for implementing NLO calculations in shower Monte Carlo programs: the POWHEG BOX*, JHEP **06** (2010) 043, arXiv: 1002.2581 [hep-ph] (cit. on p. 4).

[50] J. M. Campbell, R. K. Ellis, P. Nason and E. Re, *Top-pair production and decay at NLO matched with parton showers*, JHEP **04** (2015) 114, arXiv: 1412.1828 [hep-ph] (cit. on p. 4).

[51] R. D. Ball et al., *Parton distributions for the LHC Run II*, JHEP **04** (2015) 040, arXiv: 1410.8849 [hep-ph] (cit. on pp. 4, 14).

[52] ATLAS Collaboration, *Studies on top-quark Monte Carlo modelling for Top2016*, ATL-PHYS-PUB-2016-020, 2016, URL: https://cds.cern.ch/record/2216168 (cit. on pp. 4, 5).

[53] T. Sjöstrand et al., *An introduction to PYTHIA 8.2*, Comput. Phys. Commun. **191** (2015) 159, arXiv: 1410.3012 [hep-ph] (cit. on p. 4).

[54] M. Czakon and A. Mitov, *Top++: A program for the calculation of the top-pair cross-section at hadron colliders*, Comput. Phys. Commun. **185** (2014) 2930, arXiv: 1112.5675 [hep-ph] (cit. on p. 4).

[55] M. Cacciari, M. Czakon, M. Mangano, A. Mitov and P. Nason, *Top-pair production at hadron colliders with next-to-next-to-leading logarithmic soft-gluon resummation*, Phys. Lett. B **710** (2012) 612, arXiv: 1111.5869 [hep-ph] (cit. on p. 4).

[56] P. Bärnreuther, M. Czakon and A. Mitov, *Percent Level Precision Physics at the Tevatron: First Genuine NNLO QCD Corrections to $q\bar{q} \to t\bar{t} + X$*, Phys. Rev. Lett. **109** (2012) 132001, arXiv: 1204.5201 [hep-ph] (cit. on p. 4).

[57] M. Czakon and A. Mitov, *NNLO corrections to top-pair production at hadron colliders: the all-fermionic scattering channels*, JHEP **12** (2012) 054, arXiv: 1207.0236 [hep-ph] (cit. on p. 4).

[58] M. Czakon, P. Fiedler and A. Mitov, *Total Top-Quark Pair-Production Cross Section at Hadron Colliders Through $O(\alpha_S^4)$*, Phys. Rev. Lett. **110** (2013) 252004, arXiv: 1303.6254 [hep-ph] (cit. on p. 4).

[59] R. Frederix, E. Re and P. Torrielli, *Single-top t-channel hadroproduction in the four-flavour scheme with POWHEG and aMC@NLO*, JHEP **09** (2012) 130, arXiv: 1207.5391 [hep-ph] (cit. on pp. 4, 13).

[60] S. Frixione, E. Laenen, P. Motylinski, C. D. White and B. R. Webber, *Single-top hadroproduction in association with a W boson*, JHEP **07** (2008) 029, arXiv: 0805.3067 [hep-ph] (cit. on pp. 4, 13).

[61] T. Gleisberg and S. Höche, *Comix, a new matrix element generator*, JHEP **12** (2008) 039, arXiv: 0808.3674 [hep-ph] (cit. on p. 4).

[62] F. Cascioli, P. Maierhöfer and S. Pozzorini, *Scattering Amplitudes with Open Loops*, Phys. Rev. Lett. **108** (2012) 111601, arXiv: 1111.5206 [hep-ph] (cit. on p. 4).

[63] A. Denner, S. Dittmaier and L. Hofer, *Collier: a fortran-based Complex One-Loop LIbrary in Extended Regularizations*, Comput. Phys. Commun. **212** (2017) 220, arXiv: 1604.06792 [hep-ph] (cit. on p. 4).

[64] S. Schumann and F. Krauss, *A parton shower algorithm based on Catani–Seymour dipole factorisation*, JHEP **03** (2008) 038, arXiv: 0709.1027 [hep-ph] (cit. on pp. 4, 5).

[65] J.-C. Winter, F. Krauss and G. Soff, *A Modified cluster hadronization model*, Eur. Phys. J. C **36** (2004) 381, arXiv: hep-ph/0311085 [hep-ph] (cit. on pp. 4, 5).

[66] S. Hoeche, F. Krauss, M. Schonherr and F. Siegert, *A critical appraisal of NLO+PS matching methods*, JHEP **09** (2012) 049, arXiv: 1111.1220 [hep-ph] (cit. on p. 4).

[67] S. Catani, F. Krauss, R. Kuhn and B. R. Webber, *QCD matrix elements + parton showers*, JHEP **11** (2001) 063, arXiv: hep-ph/0109231 [hep-ph] (cit. on p. 4).

[68] S. Höche, F. Krauss, S. Schumann and F. Siegert, *QCD matrix elements and truncated showers*, JHEP **05** (2009) 053, arXiv: 0903.1219 [hep-ph] (cit. on p. 4).

[69] S. Höche, F. Krauss, M. Schönherr and F. Siegert, *QCD matrix elements + parton showers. The NLO case*, JHEP **04** (2013) 027, arXiv: 1207.5030 [hep-ph] (cit. on p. 4).

[70] E. Bothmann et al., *Event Generation with Sherpa 2.2*, SciPost Phys. **7** (2019) 034, arXiv: 1905.09127 [hep-ph] (cit. on p. 4).

[71] H. B. Hartanto, B. Jager, L. Reina and D. Wackeroth, *Higgs boson production in association with top quarks in the POWHEG BOX*, Phys. Rev. **D91** (2015) 094003, arXiv: 1501.04498 [hep-ph] (cit. on p. 4).

[72] A. Denner, S. Dittmaier, M. Roth and M. Weber, *Electroweak radiative corrections to e+ e- —> nu anti-nu H*, Nucl. Phys. B **660** (2003) 289, arXiv: hep-ph/0302198 (cit. on p. 5).

[73] ATLAS Collaboration, *The ATLAS Simulation Infrastructure*, Eur. Phys. J. C **70** (2010) 823, arXiv: 1005.4568 [physics.ins-det] (cit. on p. 5).

[74] S. Agostinelli et al., *GEANT4 – a simulation toolkit*, Nucl. Instrum. Meth. A **506** (2003) 250 (cit. on p. 5).

[75] ATLAS Collaboration, *The simulation principle and performance of the ATLAS fast calorimeter simulation FastCaloSim*, ATL-PHYS-PUB-2010-013, 2010, URL: https://cds.cern.ch/record/1300517 (cit. on p. 5).

[76] D. J. Lange, *The EvtGen particle decay simulation package*, Nucl. Instrum. Meth. A **462** (2001) 152 (cit. on p. 5).

[77] ATLAS Collaboration, *Electron and photon performance measurements with the ATLAS detector using the 2015–2017 LHC proton–proton collision data*, JINST **14** (2019) P12006, arXiv: 1908.00005 [hep-ex] (cit. on p. 6).

[78] ATLAS Collaboration, *Electron efficiency measurements with the ATLAS detector using the 2015 LHC proton–proton collision data*, ATLAS-CONF-2016-024, 2016, URL: https://cds.cern.ch/record/2157687 (cit. on p. 6).

[79] ATLAS Collaboration, *Muon reconstruction performance of the ATLAS detector in proton–proton collision data at* $\sqrt{s} = 13$ *TeV*, Eur. Phys. J. C **76** (2016) 292, arXiv: 1603.05598 [hep-ex] (cit. on pp. 6, 12).

[80] ATLAS Collaboration, *Topological cell clustering in the ATLAS calorimeters and its performance in LHC Run 1*, Eur. Phys. J. C **77** (2017) 490, arXiv: 1603.02934 [hep-ex] (cit. on p. 6).

[81] M. Cacciari, G. P. Salam and G. Soyez, *The anti-k_t jet clustering algorithm*, JHEP **04** (2008) 063, arXiv: 0802.1189 [hep-ph] (cit. on p. 6).

[82] ATLAS Collaboration, *Jet energy scale measurements and their systematic uncertainties in proton–proton collisions at* $\sqrt{s} = 13$ *TeV with the ATLAS detector*, Phys. Rev. D **96** (2017) 072002, arXiv: 1703.09665 [hep-ex] (cit. on pp. 6, 12).

[83] ATLAS Collaboration, *Selection of jets produced in* 13 *TeV proton–proton collisions with the ATLAS detector*, ATLAS-CONF-2015-029, 2015, URL: https://cds.cern.ch/record/2037702 (cit. on p. 6).

[84] ATLAS Collaboration, *Performance of pile-up mitigation techniques for jets in pp collisions at $\sqrt{s}$ = 8 TeV using the ATLAS detector*, Eur. Phys. J. C **76** (2016) 581, arXiv: 1510.03823 [hep-ex] (cit. on pp. 6, 12).

[85] ATLAS Collaboration, *Measurements of b-jet tagging efficiency with the ATLAS detector using $t\bar{t}$ events at $\sqrt{s}$ = 13 TeV*, JHEP **08** (2018) 089, arXiv: 1805.01845 [hep-ex] (cit. on p. 6).

[86] ATLAS Collaboration, *ATLAS b-jet identification performance and efficiency measurement with $t\bar{t}$ events in pp collisions at $\sqrt{s}$ = 13 TeV*, Eur. Phys. J. C **79** (2019) 970, arXiv: 1907.05120 [hep-ex] (cit. on pp. 6, 12).

[87] ATLAS Collaboration, *Performance of missing transverse momentum reconstruction with the ATLAS detector in the first proton–proton collisions at $\sqrt{s}$ = 13 TeV*, ATL-PHYS-PUB-2015-027, 2015, URL: https://cds.cern.ch/record/2037904 (cit. on p. 7).

[88] ATLAS Collaboration, *Improvements in $t\bar{t}$ modelling using NLO+PS Monte Carlo generators for Run 2*, ATL-PHYS-PUB-2018-009, 2018, URL: https://cds.cern.ch/record/2630327 (cit. on p. 7).

[89] ATLAS Collaboration, *Measurements of top-quark pair single- and double-differential cross-sections in the all-hadronic channel in pp collisions at $\sqrt{s}$ = 13 TeV using the ATLAS detector*, 2020, arXiv: 2006.09274 [hep-ex] (cit. on p. 7).

[90] F. Chollet et al., *Keras*, https://keras.io, 2015 (cit. on p. 10).

[91] D. P. Kingma and J. Ba, *Adam: A Method for Stochastic Optimization*, 2014, arXiv: 1412.6980 [cs.LG] (cit. on p. 10).

[92] P. Baldi, K. Cranmer, T. Faucett, P. Sadowski and D. Whiteson, *Parameterized neural networks for high-energy physics*, Eur. Phys. J. C **76** (2016) 235, arXiv: 1601.07913 [hep-ex] (cit. on p. 10).

[93] G. C. Fox and S. Wolfram, *Event Shapes in e+ e- Annihilation*, Nucl. Phys. B **149** (1979) 413 (cit. on p. 10), Erratum: Nucl. Phys. B **157** (1979) 543.

[94] ATLAS Collaboration, *Luminosity determination in pp collisions at $\sqrt{s}$ = 13 TeV using the ATLAS detector at the LHC*, ATLAS-CONF-2019-021, 2019, URL: https://cds.cern.ch/record/2677054 (cit. on p. 11).

[95] G. Avoni et al., *The new LUCID-2 detector for luminosity measurement and monitoring in ATLAS*, JINST **13** (2018) P07017 (cit. on p. 11).

[96] ATLAS Collaboration, *Measurement of the Inelastic Proton–Proton Cross Section at $\sqrt{s}$ = 13 TeV with the ATLAS Detector at the LHC*, Phys. Rev. Lett. **117** (2016) 182002, arXiv: 1606.02625 [hep-ex] (cit. on p. 11).

[97] ATLAS Collaboration, *Electron reconstruction and identification in the ATLAS experiment using the 2015 and 2016 LHC proton–proton collision data at $\sqrt{s}$ = 13 TeV*, Eur. Phys. J. C **79** (2019) 639, arXiv: 1902.04655 [hep-ex] (cit. on p. 12).

[98] ATLAS Collaboration, *Determination of jet calibration and energy resolution in proton–proton collisions at $\sqrt{s}$ = 8 TeV using the ATLAS detector*, (2019), arXiv: 1910.04482 [hep-ex] (cit. on p. 12).

[99] ATLAS Collaboration, *Measurement of b-tagging efficiency of c-jets in $t\bar{t}$ events using a likelihood approach with the ATLAS detector*, ATLAS-CONF-2018-001, 2018, URL: https://cds.cern.ch/record/2306649 (cit. on p. 12).

[100] ATLAS Collaboration, *Calibration of light-flavour b-jet mistagging rates using ATLAS proton–proton collision data at* $\sqrt{s}$ = 13 *TeV*, ATLAS-CONF-2018-006, 2018, URL: https://cds.cern.ch/record/2314418 (cit. on p. 12).

[101] ATLAS Collaboration, *Performance of missing transverse momentum reconstruction with the ATLAS detector using proton–proton collisions at* $\sqrt{s}$ = 13 *TeV*, Eur. Phys. J. C **78** (2018) 903, arXiv: 1802.08168 [hep-ex] (cit. on p. 12).

[102] ATLAS Collaboration, E_T^{miss} *performance in the ATLAS detector using 2015–2016 LHC pp collisions*, ATLAS-CONF-2018-023, 2018, URL: https://cds.cern.ch/record/2625233 (cit. on p. 12).

[103] J. Butterworth et al., *PDF4LHC recommendations for LHC Run II*, J. Phys. G **43** (2016) 023001, arXiv: 1510.03865 [hep-ph] (cit. on p. 12).

[104] LHCTopWG, *ATLAS-CMS recommended predictions for top-quark-pair cross sections*, URL: https://twiki.cern.ch/twiki/bin/view/LHCPhysics/TtbarNNLO (cit. on p. 12).

[105] LHCTopWG, *ATLAS-CMS recommended predictions for single-top cross sections*, URL: https://twiki.cern.ch/twiki/bin/view/LHCPhysics/SingleTopRefXsec (cit. on p. 13).

[106] A. D. Martin, W. J. Stirling, R. S. Thorne and G. Watt, *Parton distributions for the LHC*, Eur. Phys. J. C **63** (2009) 189, arXiv: 0901.0002 [hep-ph] (cit. on p. 13).

[107] A. D. Martin, W. J. Stirling, R. S. Thorne and G. Watt, *Uncertainties on alpha(S) in global PDF analyses and implications for predicted hadronic cross sections*, Eur. Phys. J. C **64** (2009) 653, arXiv: 0905.3531 [hep-ph] (cit. on p. 13).

[108] M. Aliev et al., *HATHOR: HAdronic Top and Heavy quarks crOss section calculatoR*, Comput. Phys. Commun. **182** (2011) 1034, arXiv: 1007.1327 [hep-ph] (cit. on p. 13).

[109] P. Kant et al., *HatHor for single top-quark production: Updated predictions and uncertainty estimates for single top-quark production in hadronic collisions*, Comput. Phys. Commun. **191** (2015) 74, arXiv: 1406.4403 [hep-ph] (cit. on p. 13).

[110] R. Raitio and W. W. Wada, *Higgs Boson Production at Large Transverse Momentum in QCD*, Phys. Rev. D **19** (1979) 941 (cit. on p. 14).

[111] W. Beenakker et al., *NLO QCD corrections to t anti-t H production in hadron collisions*, Nucl. Phys. B **653** (2003) 151, arXiv: hep-ph/0211352 [hep-ph] (cit. on p. 14).

[112] S. Dawson, C. Jackson, L. H. Orr, L. Reina and D. Wackeroth, *Associated Higgs production with top quarks at the large hadron collider: NLO QCD corrections*, Phys. Rev. D **68** (2003) 034022, arXiv: hep-ph/0305087 [hep-ph] (cit. on p. 14).

[113] Y. Zhang, W.-G. Ma, R.-Y. Zhang, C. Chen and L. Guo, *QCD NLO and EW NLO corrections to* $t\bar{t}H$ *production with top quark decays at hadron collider*, Phys. Lett. B **738** (2014) 1, arXiv: 1407.1110 [hep-ph] (cit. on p. 14).

[114] S. Frixione, V. Hirschi, D. Pagani, H.-S. Shao and M. Zaro, *Electroweak and QCD corrections to top-pair hadroproduction in association with heavy bosons*, JHEP **06** (2015) 184, arXiv: 1504.03446 [hep-ph] (cit. on p. 14).

[115] J. M. Campbell and R. K. Ellis, $t\bar{t}W^{\pm}$ *production and decay at NLO*, JHEP **07** (2012) 052, arXiv: 1204.5678 [hep-ph] (cit. on p. 14).

[116] R. Frederix, D. Pagani and M. Zaro, *Large NLO corrections in $t\bar{t}W^{\pm}$ and $t\bar{t}t\bar{t}$ hadroproduction from supposedly subleading EW contributions*, JHEP **02** (2018) 031, arXiv: 1711.02116 [hep-ph] (cit. on p. 14).

[117] E. Bothmann, M. Schönherr and S. Schumann, *Reweighting QCD matrix-element and parton-shower calculations*, The European Physical Journal C **76** (2016), ISSN: 1434-6052, URL: http://dx.doi.org/10.1140/epjc/s10052-016-4430-0 (cit. on p. 14).

[118] ATLAS Collaboration, *Multi-boson simulation for* 13 *TeV ATLAS analyses*, ATL-PHYS-PUB-2016-002, 2016, URL: https://cds.cern.ch/record/2119986 (cit. on p. 14).

[119] G. Cowan, K. Cranmer, E. Gross and O. Vitells, *Asymptotic formulae for likelihood-based tests of new physics*, Eur. Phys. J. C **71** (2011) 1554, arXiv: 1007.1727 [physics.data-an] (cit. on p. 14), Erratum: Eur. Phys. J. C **73** (2013) 2501.

[120] A. L. Read, *Presentation of search results: the CL_S technique*, J. Phys. G **28** (2002) 2693 (cit. on p. 14).

[121] T. Junk, *Confidence level computation for combining searches with small statistics*, Nucl. Inst. and Meth. A **434** (1999) 435, ISSN: 0168-9002, URL: http://dx.doi.org/10.1016/S0168-9002(99)00498-2 (cit. on p. 14).

[122] S. Heinemeyer, W. Hollik and G. Weiglein, *FeynHiggs: A Program for the calculation of the masses of the neutral CP even Higgs bosons in the MSSM*, Comput. Phys. Commun. **124** (2000) 76, arXiv: hep-ph/9812320 (cit. on p. 15).

[123] S. Heinemeyer, W. Hollik and G. Weiglein, *The Masses of the neutral CP - even Higgs bosons in the MSSM: Accurate analysis at the two loop level*, Eur. Phys. J. C **9** (1999) 343, arXiv: hep-ph/9812472 (cit. on p. 15).

[124] G. Degrassi, S. Heinemeyer, W. Hollik, P. Slavich and G. Weiglein, *Towards high precision predictions for the MSSM Higgs sector*, Eur. Phys. J. C **28** (2003) 133, arXiv: hep-ph/0212020 (cit. on p. 15).

[125] M. Frank et al., *The Higgs Boson Masses and Mixings of the Complex MSSM in the Feynman-Diagrammatic Approach*, JHEP **02** (2007) 047, arXiv: hep-ph/0611326 (cit. on p. 15).

[126] T. Hahn, S. Heinemeyer, W. Hollik, H. Rzehak and G. Weiglein, *High-Precision Predictions for the Light CP -Even Higgs Boson Mass of the Minimal Supersymmetric Standard Model*, Phys. Rev. Lett. **112** (2014) 141801, arXiv: 1312.4937 [hep-ph] (cit. on p. 15).

[127] H. Bahl and W. Hollik, *Precise prediction for the light MSSM Higgs boson mass combining effective field theory and fixed-order calculations*, Eur. Phys. J. C **76** (2016) 499, arXiv: 1608.01880 [hep-ph] (cit. on p. 15).

[128] H. Bahl, S. Heinemeyer, W. Hollik and G. Weiglein, *Reconciling EFT and hybrid calculations of the light MSSM Higgs-boson mass*, Eur. Phys. J. C **78** (2018) 57, arXiv: 1706.00346 [hep-ph] (cit. on p. 15).

[129] A. Djouadi, J. Kalinowski and M. Spira, *HDECAY: A Program for Higgs boson decays in the standard model and its supersymmetric extension*, Comput. Phys. Commun. **108** (1998) 56, arXiv: hep-ph/9704448 (cit. on p. 15).

[130] A. Djouadi, J. Kalinowski, M. Muehlleitner and M. Spira, *HDECAY: Twenty$_{++}$ years after*, Comput. Phys. Commun. **238** (2019) 214, arXiv: 1801.09506 [hep-ph] (cit. on p. 15).

[131] A. Bredenstein, A. Denner, S. Dittmaier and M. Weber, *Precise predictions for the Higgs-boson decay H —> WW/ZZ —> 4 leptons*, Phys. Rev. D **74** (2006) 013004, arXiv: hep-ph/0604011 (cit. on p. 15).

[132] A. Bredenstein, A. Denner, S. Dittmaier and M. Weber, *Radiative corrections to the semileptonic and hadronic Higgs-boson decays H —> W W / Z Z —> 4 fermions*, JHEP **02** (2007) 080, arXiv: hep-ph/0611234 (cit. on p. 15).